An Exported Kinase Family Mediates Species-Specific Erythrocyte Remodelling and Virulence in Human Malaria

Heledd Davies[1,#], Hugo Belda[1,#], Malgorzata Broncel[1], Xingda Ye[1,2], Claudine Bisson[3], Viola Introini[4], Dominique Dorin-Semblat[5,6], Jean-Philippe Semblat[5,6], Marta Tibúrcio[1], Benoit Gamain[5,6], Myrsini Kaforou[2], Moritz Treeck[1,*]

[1] Signalling in Apicomplexan Parasites Laboratory, The Francis Crick Institute, London, United Kingdom

[2] Division of Infectious Diseases, Department of Medicine, Imperial College London, London, UK,

[4] Cavendish Laboratory, University of Cambridge, Cambridge, United Kingdom,

[3] Institute of Structural and Molecular Biology, Birkbeck College, University of London, London, UK.

[5] Université de Paris, Biologie Intégrée du Globule Rouge, UMR_S1134, BIGR, INSERM, F-75015, Paris, France.

[6] Institut National de la Transfusion Sanguine, F-75015, Paris, France.

[#] These authors contributed equally

[*] Corresponding author and lead contact

Correspondence to: moritz.treeck@crick.ac.uk

Summary

The most severe form of human malaria is caused by *Plasmodium falciparum*. Its virulence is closely linked to the increase in rigidity and cytoadhesion of infected erythrocytes, which obstruct blood flow to vital organs. Unlike other human-infecting *Plasmodium* species, *P. falciparum* exports a family of 18 'FIKK' serine/threonine kinases of unknown function into the host cell. We reveal substantial species-specific phosphorylation of erythrocyte proteins by *P. falciparum*, but not by *Plasmodium knowlesi*, which is not predicted to export any kinases. By systematic deletion of all FIKK kinases combined with large-scale quantitative phosphoproteomics we identify unique phosphorylation fingerprints for each kinase, including phosphosites on parasite virulence factors and host cell proteins. We subsequently show that one kinase, FIKK4.1, mediates both cytoskeletal rigidification and trafficking of the adhesin and key virulence factor PfEMP1 to the host cell surface. This establishes the FIKK family as important drivers of parasite evolution, and malaria pathology.

Introduction:

Humans are infected by at least five *Plasmodium* species that cause malaria, of which *Plasmodium falciparum* is responsible for the most debilitating form of the disease. Red blood cells (RBCs) infected by *P. falciparum* become more rigid and cytoadhere to the host vascular endothelium and other cells, avoiding clearance of infected cells by the spleen and leading to severe complications for the patient. Cytoadhesion is mediated by a multigene family of *P. falciparum* Erythrocyte Membrane Protein 1 (PfEMP1), which is inserted into protrusions on the RBC surface called "knobs" [1]. Only one of the ~60 PfEMP1 variants is expressed at a given time, determining adhesion to a specific host receptor. For example, the gene *var2csa* encodes a PfEMP1 variant that binds to CSA on the placenta [2]. Other human-infecting Plasmodium species do not express PfEMP1, and the symptoms of infection are usually much milder in patients infected by these parasites.

Approximately 600 proteins are predicted to be exported into the host cell by the parasite to mediate RBC remodelling [3-5]. Membranous vacuoles called Maurer's clefts help traffic proteins such as PfEMP1 to the cell surface [6], assisted by PfEMP1 trafficking proteins (PTPs) [7]. Other proteins are involved in anchoring PfEMP1 to the RBC cytoskeleton [8,9], which is composed of a flexible network of spectrin filaments connected to the plasma membrane by the ankyrin complex and the 4.1R complex [10,11]. Parasite proteins interacting with the RBC cytoskeleton include KAHRP, a major component of the knob structures, which is also involved in host cell rigidification [12,13].

The FIKK kinases are a family of 18-26 serine/threonine kinases which are exported into the host cell by *Plasmodium* parasites of the *Laverania* clade, which includes *P. falciparum* and other great ape infecting species [14-16]. Other less pathogenic *Plasmodium* species are not predicted to export kinases into the host cell and possess just one ancestral FIKK kinase, named FIKK8 in *P. falciparum*, which is not exported [17]. *P. falciparum* is predicted to export 20 FIKKs into the host cell, although two of these are pseudogenes [15,18]. The FIKKs contain a variable N-terminal region and a highly conserved kinase domain which lacks the canonical glycine-rich ATP-binding motif, but contains a Phe-Ile-Lys-Lys motif of unknown function located N-terminal to the kinase domain, for which they are named. Despite this atypical kinase domain, all FIKK kinases assayed so far have been demonstrated to be enzymatically active [18-21], and some have been implicated in modulating RBC properties [21,22], but their substrates remain unknown. Most FIKKs remain highly conserved across *Laverania* species, predicting an important function in host-pathogen interaction [23]. We hypothesise that the FIKK kinase family expanded and gained an export element for

transport into the host cell to mediate the RBC remodelling responsible for the particular virulence of *P. falciparum*.

Here we provide the first large-scale quantitative phosphoproteome of human RBCs infected with two different malaria species, *P. falciparum* and *P. knowlesi*. We reveal substantial species-specific phosphorylation of RBC proteins almost exclusively in *P. falciparum* infected RBCs (Pf iRBCs). Deep phosphoproteome profiling of knockout lines for all exported FIKK kinases provides a detailed map of phosphorylation events controlled by each kinase, confirming that the FIKK kinases are key regulators of *P. falciparum*-specific changes to RBCs which are linked to severe malaria. Guided by the enrichment of phosphosites regulated by FIKK4.1 on cytoskeletal proteins and proteins involved in PfEMP1 trafficking, we demonstrate an important function for this kinase in controlling rigidity and cytoadhesion.

Results:

Phosphorylation of RBC proteins is *P. falciparum*-specific

The presence of exported FIKK kinases in *P. falciparum,* but not in other human-infecting *Plasmodium* species suggests that FIKK kinase activity plays a species-specific role in modulating RBC proteins (Figure 1A). To test this, we compared the phosphoproteome of RBCs infected with *P. falciparum* to that of a *P. knowlesi* strain adapted for culture in human RBCs [24] (Figure 1B for experimental workflow). As a control, we also determined the phosphoproteome of uninfected RBCs (uRBCs) cultured under the same conditions. We purified iRBCs from uRBCs by magnetic separation; late stage parasites are retained on a column in a magnetic field due to the presence of paramagnetic hemozoin that is formed upon ingestion of haemoglobin, while uRBCs and the younger ring stages pass through. Parasite samples were collected at schizont stage, at ~44 hours post infection (hpi) for *P. falciparum* and ~24hpi for *P. knowlesi*. Ten samples were analysed by mass spectrometry using Ten-plex Tandem Mass Tags (TMT) to quantify phosphosite occupancy [25], including technical triplicates of *P. falciparum* and *P. knowlesi* iRBCs and uRBCs combined from both cultures, as well as one uRBC sample from the *P. falciparum* culture only. These were lysed, digested, and labelled with TMT labels. Phosphopeptides were enriched and fractionated, then analysed by two different mass spectrometry methods (MS2 and MS3) on two different instruments.

We observed a substantial increase in ser/thr phosphorylation of RBC proteins in *P. falciparum* iRBCs compared to uRBCs (Figure 1C and Table S1). Using a threshold based on the log2 fold change (L2FC) and the *P*-value, 99 phosphosites showed a significant increase in phosphorylation upon infection by *P.*

falciparum and 6 phosphosites showed a decrease in phosphorylation (Figure 1C panel i, and Table S2). Upon infection with *P. knowlesi*, only 24 phosphosites showed an increase in phosphorylation while 9 decreased (Figure 1C panel ii). To directly correlate the protein residues phosphorylated by the different species, we plotted the L2FC (iRBCs/uRBCs) for both *P. falciparum* and *P. knowlesi* in a concordance-discordance (DISCO) plot (Figure 1D). This illustrates that while some residues are phosphorylated more when infected with either parasite species, possibly due to host kinases responding to the altered cell environment (Figure 1D, green box), many more residues are phosphorylated more upon infection with *P. falciparum* only (Figure 1D, blue box). Notably, 53% of the residues phosphorylated in *P. falciparum* only are novel (PhosphoSitePlus), indicating that these may be phosphorylated by *P. falciparum* FIKK kinases.

To test whether phosphorylation of RBC proteins is affected by different host environments, we compared the phosphoproteome of *P. falciparum* cultured for one cycle in blood from three different donors with different blood types, A+, AB+ or O+ (Figure 1E for experimental workflow). To ensure the parasites were collected at the same time points, we designed a magnetic purification stand with capacity for 5 medium-sized magnetic columns (MACS CS), based on a design by Kim *et. al* [26]. We observed very few differences between the phosphoproteomes of the three blood types in either uninfected or infected RBCs (one way ANOVA testing [F(2,1527) = 0.322, *P*-value = 0.724 (NS))](Figure 1F, Figure S1A, S1B and Table S2). This allows us to compare RBC phosphoproteomes across experiments where different blood samples are used.

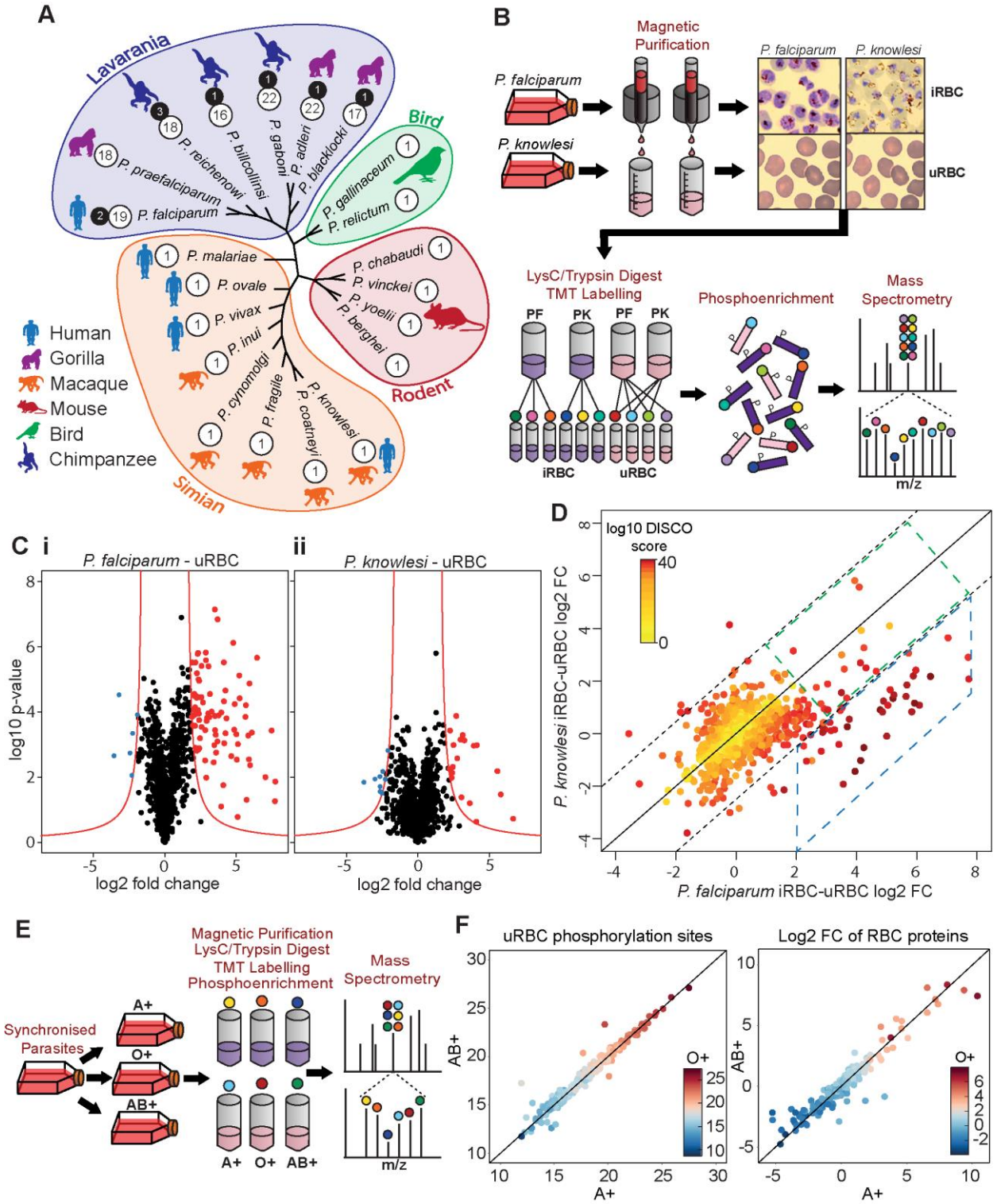

Figure 1: Infection of RBCs with *P. falciparum* or *P. knowlesi* induces species-specific changes to the phosphoproteome of RBC proteins independently of blood type. (A) Maximum likelihood phylogenetic tree of *Plasmodium* species, with clades grouped together. Silhouettes show host specificity. Divergence was calculated on the sequences of FIKK8 from each species. Numbers in white circles are the number of active FIKKs, black circles are pseudogenes. **(B)** Experimental workflow for phosphoproteomics of *P. falciparum* and *P. knowlesi*-iRBCs. Coloured circles represent the ten tandem mass tags. **(C)** Volcano plots depicting the L2FC (x axis) in phosphosite intensity between uRBCs and iRBCs with *P. falciparum* (i) and *P. knowlesi* (ii). A positive L2FC indicates that a protein residue site is more phosphorylated in iRBCs. y axis = log10 *P*-value between 3 technical replicates. **(D)** DISCO plot

representing *P. falciparum*/uRBCs L2FC (y axis) vs *P. knowlesi*/uRBCs L2FC. Colour – discordance score (yellow - low, red - high). Green box – phosphosites more phosphorylated in both *P. falciparum* and *P. knowlesi*-iRBCs. Blue box – phosphosites more phosphorylated in *P. falciparum*-iRBCs only (for indication purposes only, not considering the *P*-value). **(E)** Experimental workflow for phosphoproteomics of *P. falciparum* in different blood types. **(F)** Comparison of the phosphoproteome of three different blood types, A+ (x axis), AB+ (y axis) and O+ (colour scale). Left – uRBC phosphorylation intensity, Right – L2FC in RBC protein phosphosite intensity between uRBCs and *P. falciparum*-iRBCs. See also Figure S1 and Table S2.

Systematic conditional deletion of FIKK kinases

We hypothesised that FIKK kinases may mediate phosphorylation events observed in *P. falciparum* but not in *P. knowlesi* iRBCs. To identify the substrates of the FIKK kinases, we generated conditional gene knockouts (cKO) for all 19 FIKKs. We targeted 12 FIKK kinases individually (FIKK1, 3, 4.1, 4.2, 5, 7.1, 8, 10.1, 10.2, 11, 12, 13) by flanking their kinase domains with two artificial introns containing LoxP sites (LoxPint) and introducing a C-terminal HA-tag in the same modification step, as previously described [27]. Integration into the endogenous locus was either enhanced using a selection-linked integration (SLI) method [28] (Figure 2A), or by targeting the endogenous locus with CRISPR/Cas9 (Figure S2).

The remaining 7 FIKK kinases are located in a cluster on chromosome 9. For these, we introduced two LoxPints into *fikk9.1* and *fikk9.7* genes in a single transfection step using a CRISPR/Cas9 strategy where two guide RNAs are expressed from a single plasmid (Figure 2B). To enhance the excision efficiency we introduced a Neomycin resistance cassette which would move into frame with the N-terminus of *fikk9.7* upon correct excision of *fikk9.1-9.7* (FIKK9s). All constructs were transfected into an NF54::DiCre line that allows for phenotyping in all lifecycle stages (unpublished). Five FIKKs (FIKK4.1, 7.1, 8, 10.1, 11) were additionally transfected into a 1G5::DiCre line [29]. All parasite lines were cloned [30] and correct integration of constructs was verified by PCR (Figure S2).

Western blot analysis of cKO FIKK lines showed HA-positive bands of various intensities at the predicted sizes (Figure 2C). FIKK7.1 was only detectable after concentration by HA-immunoprecipitation (Figure 2C, far right panel), and FIKK13 was not detectable under any conditions. We observed an additional protein band approximately 25kDa above the predicted size for most FIKKs, which is likely a result of incorrect skipping of the 2A peptide, leading to a minor population of a FIKK-Neomycin fusion protein. RAP-mediated excision of the FIKK kinases was confirmed by the loss of the HA-positive band 72h after treatment (Figure 2C). This was further confirmed by PCR (Figure S2). For the FIKK9 cluster, some of the non-recombined locus as well as the excised episome persisted up to 12 days after RAP treatment, as indicated by PCR

(Figure S2). We therefore selected for excised parasites using neomycin and obtained clones to verify the absence of FIKK9s by western blot and PCR (Figure 2C and Figure S2).

We next compared the growth rates of DMSO and RAP treated FIKK cKO lines along with the NF54::DiCre parental line by flow cytometry over 96 hours. While for the non-exported FIKK8 we observed a significant drop in growth, no significant difference could be observed for any exported FIKK lines over this time period (Figure S3). The C-terminal HA-tag fused to each kinase allowed us to visualize their subcellular localisation. FIKKs which showed very low expression levels by Western blot were also not identifiable by IFA. As expected, FIKK8 was not exported and localised within the parasite. All other FIKKs we could detect by immunofluorescence assay (IFA) showed export into the host cell, with some remaining within the parasite. FIKK 1, FIKK10.1 and FIKK10.2 co-localised with the Maurer's Cleft marker MAHRP1, whereas FIKK4.1 and FIKK4.2 strongly co-localised with KAHRP at the RBC periphery (Figure 2D).

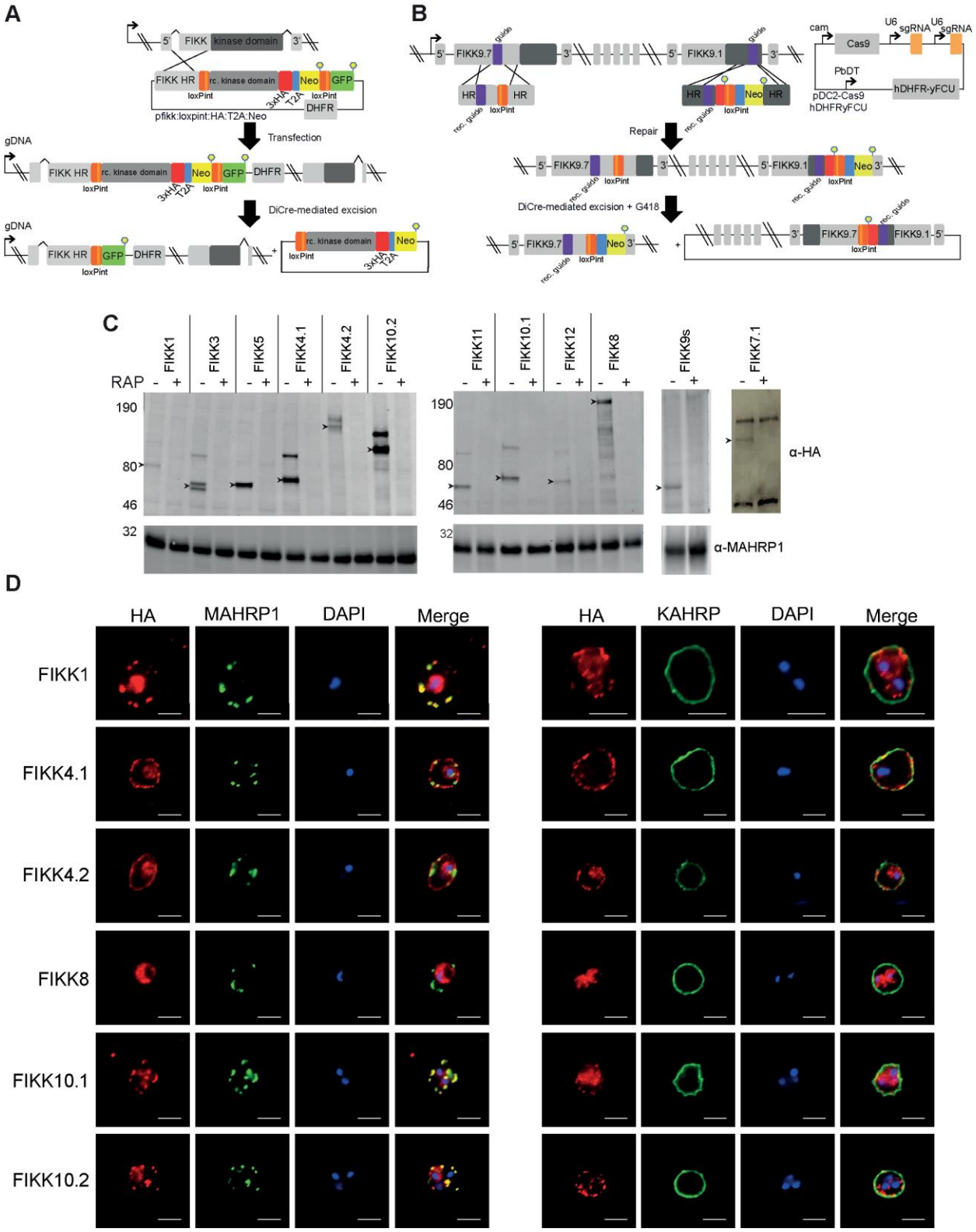

Figure 2: FIKK cKO strategies allow for efficient excision upon RAP treatment and localisation. **(A)** Description of the FIKK cKO strategy using the SLI method (Birnbaum, 2017). Schematic shows the structure of the *fikk* locus after integration and after Cre-mediated excision. **(B)** CRISPR/Cas9-mediated introduction of LoxPints into the *fikk9.1* and *fikk9.7* loci. RAP-treatment induces excision of all FIKKs located on chromosome 9 and expression of the Neomycin resistance cassette. **(C)** Western blots confirming correct expression and excision of FIKK kinases upon RAP-treatment. MAHRP1 antibody (bottom panel) demonstrates equal loading. FIKK7.1 samples were obtained by HA immunoprecipitation. **(D)** Subcellular

localisation pattern of a selection of FIKK kinases using antibodies against the C-terminal HA-tag fused to each FIKK kinase, MAHRP1 (Maurer's cleft marker), and KAHRP (knob marker). DAPI was used for nuclear staining. Scale bar = 5µm. See also Figure S2.

FIKK kinases show non-redundant phosphorylation fingerprints

To investigate the substrates of each FIKK kinase, we tightly synchronised the FIKK cKO lines and treated with either RAP or DMSO at ring stage. Samples were then enriched by magnet in the next cycle at late schizont stage (Figure 3A). Four quantitative phosphoproteome experiments using 10-plex TMT reagents were performed (see Table S1 for an overview), two of which also included RBCs infected with NF54 or *P. knowlesi*. L2FC were calculated based on the difference between intensity values of the reporter ions in DMSO and RAP-treated lines, and averaged between replicated lines.

Deletion of each FIKK kinase affected the level of phosphorylation on both RBC and *P. falciparum* proteins (Figure 3B and Table S3). The number of significantly changing phosphosites varied between FIKKs and generally correlated with the expression level of the kinase; deletion of highly expressed FIKK4.1 and FIKK10.2 resulted in the highest levels of differential phosphorylation while deletion of the barely detectable FIKK7.1 and FIKK13 affected very few phosphosites. For FIKK1, FIKK4.1, FIKK9s and FIKK10.2, more than half the residues less phosphorylated upon FIKK deletion are on proteins predicted to be exported into the host cell (Figure 3B, red circles). Furthermore, there is a clear pattern in the subcellular localisation of many of the differentially phosphorylated proteins, with deletion of FIKK10.2 and FIKK9s affecting mostly Maurer's cleft proteins (Figure 3B, pie charts).

Unexpectedly, deletion of some FIKKs resulted in an increase in phosphorylation on several phosphosites, particularly for FIKK1 and FIKK3. These FIKKs may regulate other kinases or phosphatases or FIKK deletion may result in protein mis-localisation allowing phosphorylation by other kinases. Reassuringly, deletion of FIKK4.1, FIKK4.2, FIKK9.3, FIKK 10.1, FIKK10.2, and FIKK12 resulted in a reduction in phosphorylation on the kinase itself, either due to its truncation or loss of autophosphorylation. Interestingly, phosphorylation of FIKK10.2 was also dependent on FIKK1, suggesting one kinase may regulate the other.

To better visualise the relationships between the FIKK kinases, we assembled heatmaps representing the L2FC (DMSO/RAP) of phosphosites which were observed across all four datasets and which were significantly less phosphorylated upon deletion of at least one FIKK kinase (Figure 3C). A distinct fingerprint is observed for each FIKK kinase, demonstrating that FIKKs have largely non-overlapping functions. As expected, most FIKK-dependent phosphosites are not phosphorylated in *P. knowlesi* iRBCs. Of the 31 phosphosites significantly changing between RBCs infected by *P. falciparum* and *P. knowlesi* which were

observed in all four experiments, 22 were also affected by FIKK deletion (Figure 3D), indicating that the export of FIKK kinases is primarily responsible for the difference in RBC phosphorylation between species. Adducin S726 was previously observed to be phosphorylated upon infection by *P. falciparum*, but was believed to be a substrate of protein kinase C as it conforms to its preferred phosphorylation motif [31]. Our data suggested that this is instead mediated by FIKK1. We tested this by Western Blot using antibodies specific to adducin p726 and samples obtained from uRBCs and RBCs infected with *P. falciparum*, *P. knowlesi,* FIKK1 and FIKK4.1 DMSO and RAP-treated parasites. The results, as predicted, showed near complete dependency of adducin S726 phosphorylation on FIKK1 (Figure 3E), supporting the validity of the mass-spectrometry data.

We performed a network analysis to show the relationship between FIKKs acting on both human and exported parasite proteins (Figure 4). This revealed that some FIKKs are acting, directly or indirectly, on the same proteins. For example, deletion of 9 different FIKK kinases influences the phosphorylation of residues on Pf332, a megadalton protein which is important for Maurer's cleft morphology. Some phosphosites show opposite effects upon deletion of different kinases. For example, 5 out of 6 of the PfEMP1 trafficking proteins (PTP2, PTP3, PTP4, PTP5, and PTP6) are either more or less phosphorylated upon deletion of several FIKKs, indicating that PfEMP1 trafficking may be mediated by multiple kinases. Collectively, these data suggest that while FIKKs appear to target distinct phosphosites, they are part of a complex network and many FIKKs may act together in the same pathways.

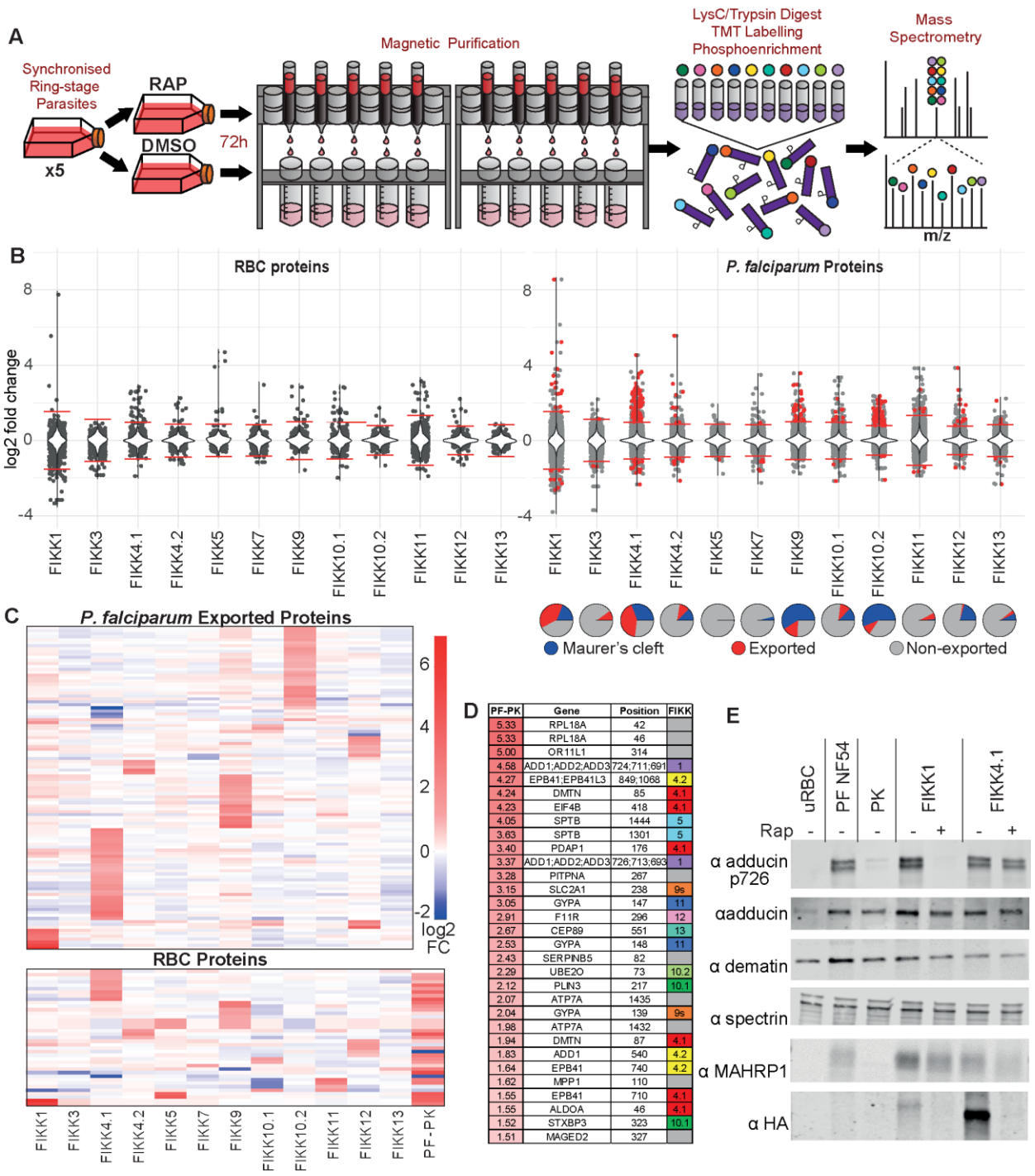

PF-PK	Gene	Position	FIKK
5.33	RPL18A	42	
5.33	RPL18A	46	
5.00	OR11L1	314	
4.58	ADD1;ADD2;ADD3	724;711;691	1
4.27	EPB41;EPB41L3	849;1068	4.2
4.24	DMTN	85	4.1
4.23	EIF4B	418	4.1
4.05	SPTB	1444	5
3.63	SPTB	1301	5
3.40	PDAP1	176	4.1
3.37	ADD1;ADD2;ADD3	726;713;693	1
3.28	PITPNA	267	
3.15	SLC2A1	238	9s
3.05	GYPA	147	11
2.91	F11R	296	12
2.67	CEP89	551	13
2.53	GYPA	148	11
2.43	SERPINB5	82	
2.29	UBE2O	73	10.2
2.12	PLIN3	217	10.1
2.07	ATP7A	1435	
2.04	GYPA	139	9s
1.98	ATP7A	1432	
1.94	DMTN	87	4.1
1.83	ADD1	540	4.2
1.64	EPB41	740	4.2
1.62	MPP1	110	
1.55	EPB41	710	4.1
1.55	ALDOA	46	4.1
1.52	STXBP3	323	10.1
1.51	MAGED2	327	

Figure 3: Each FIKK kinase influences the phosphorylation of distinct phosphosites on RBC and *P. falciparum* proteins.

(A) Experimental workflow for phosphoproteomics of FIKK cKO lines. **(B)** Violin plots depicting the L2FC in phosphorylation intensity between DMSO and RAP-treated FIKK cKO lines, on RBC proteins (panel i) and *P. falciparum* proteins (panel ii). A positive L2FC indicates that phosphorylation is reduced upon FIKK-deletion. Red horizontal lines represent significance thresholds. Red points represent exported proteins which are significantly changing upon FIKK deletion. **(C)** Heatmaps representing the intensity of phosphosites identified in all four FIKK-deletion experiments which are significantly reduced upon deletion of at least one FIKK. *P. falciparum* exported proteins (top) and RBC proteins (bottom). The bottom panel includes the L2FC between *P. falciparum* and *P. knowlesi*-iRBCs across all experiments. Phosphosites (rows) are clustered by the complete linkage method with Euclidean distance measure. **(D)** Table illustrating FIKK-dependent species-specific RBC phosphorylation. Phosphosites with the highest L2FC

between *P. falciparum* and *P. knowlesi* (column 1) are labelled by any FIKK kinases which cause a significant reduction in phosphorylation upon deletion (column 4). **(E)** Western blot confirming that adducin S726 is phosphorylated only in *P. falciparum*-iRBCs and is FIKK1-dependent. Loading controls include α-adducin, dematin and spectrin for RBC loading, and MAHRP1 for *P. falciparum* infection. Anti-HA confirms excision of FIKK1 and FIKK4.1. See also Table S3.

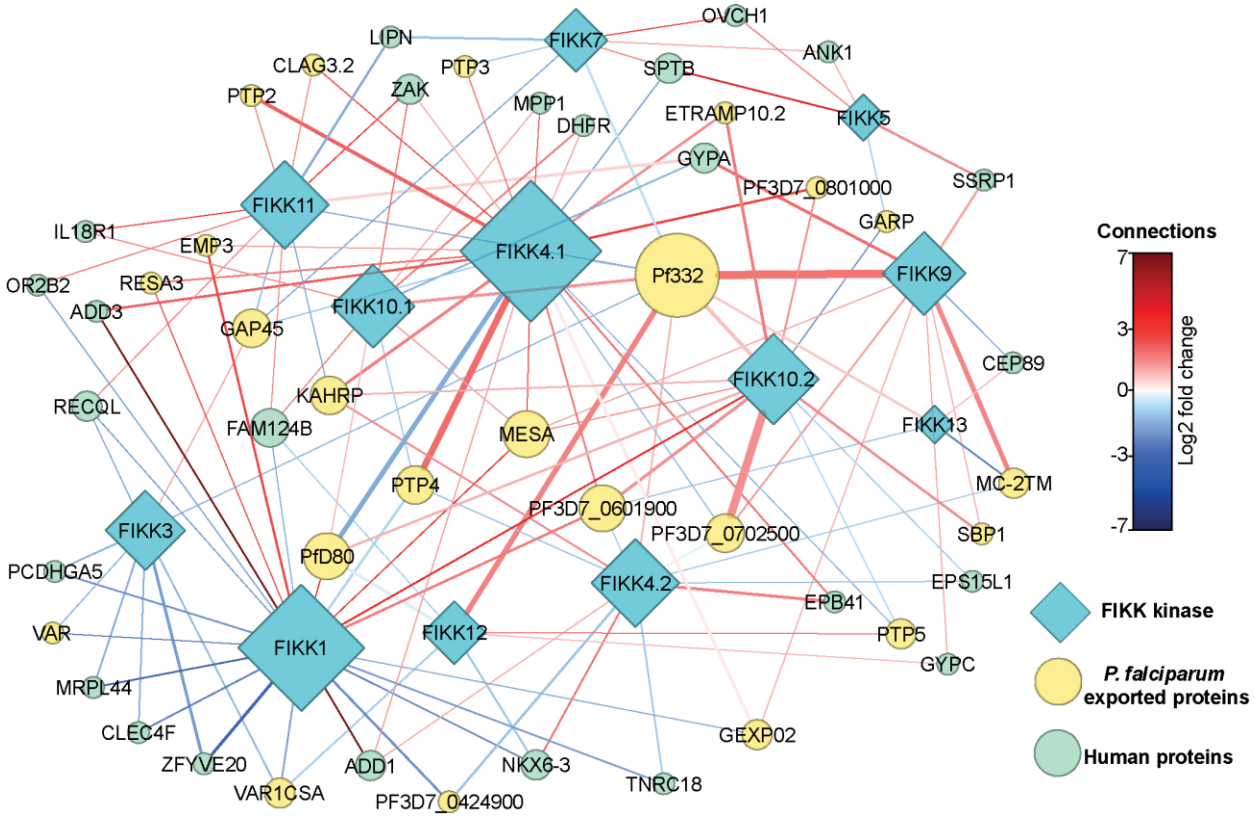

Figure 4: FIKK kinases are part of a complex network and act in synergy
Network analysis of human RBC proteins (green) and *P. falciparum* exported proteins (yellow) which are significantly changing upon deletion of the FIKK kinases (blue). The thickness of the connecting lines represents the number of phosphosites significantly changing on each protein due to each kinase deletion, while lines are coloured according to the average log2 fold change of all the significantly-changing phosphosites. Symbol size represents the number of connections to each protein.

FIKK4.1 is important for modulating RBC rigidity and cytoadhesion

A substantial concentration of the potential substrates of FIKK4.1 are on proteins known to be important for trafficking PfEMP1 to the surface of the erythrocyte and in modulating cytoadherence to host receptors and the formation of knobs[7,13,32-37]. Additionally, phosphorylation of several proteins from the 4.1R complex of the erythrocyte cytoskeleton was dependent on FIKK4.1 (Figure 5A and Table 1). We identified a very

strong enrichment for a basic phosphorylation motif with Arginine in the -3 position for FIKK4.1-dependent phosphosites, suggesting these may be direct substrates of the kinase (Figure 5B).

The 4.1R protein complex tethers the spectrin tetramers together and links the plasma membrane to the underlying cytoskeleton [10]. To test whether phosphorylation of this complex by FIKK4.1 affects the structural integrity of the RBC, we first performed membrane fluctuation analysis (flicker spectroscopy) [38,39] of RBCs infected with NF54::DiCre or FIKK4.1 cKO parasites treated with either DMSO or RAP. As described previously, a gradually increasing rigidification of the iRBC membrane is observed for all lines [39], however the FIKK4.1-deleted parasites were less rigid than the DMSO control from 32 hours post invasion onwards (Figure 5C, mean reduction in membrane tension = 25.10% at 32hpi, 26.94% at 36hpi) demonstrating that indeed FIKK4.1 is important for modulating RBC rigidity. None of the other parameters measured by flickering analysis (bending modulus, radius or viscosity) changed upon FIKK4.1 deletion (Figure S4A and B) confirming that FIKK4.1 acts specifically on the RBC cytoskeleton and not on the composition of the RBC membrane [39].

Rigidification of RBCs leads to increased retention in the spleen which can be mimicked *in vitro* by microsphiltration assays [40]. We labelled RAP-or DMSO-treated parasites with either SYBR green or Hoechst, before combining them in a 1:1 ratio and measuring the parasitemia before and after microsphiltration by flow cytometry (Figure 5D panel i). RAP-treated FIKK4.1 showed a 19.5% increase in the number of parasites passing through the beads (Figure 5D panel ii. Mean increase in the ratio of iRBCs after/before microsphiltration between DMSO and RAP = 19.5%±2.4 %; mean±SEM; n=10, including 2 replicates in 5 experiments), indicating a reduction in rigidity. Collectively these data provide strong support for an important but non-exclusive role of FIKK4.1 in modulating RBC rigidity.

The enrichment of proteins important for PfEMP1 surface translocation and knob formation among the predicted substrates of FIKK4.1 indicated that these processes may also be affected by FIKK4.1 deletion. Using qPCR, we revealed that almost all parasites within the population expressed *var2csa,* the PFEMP1 variant which binds CSA (Figure S4C). This allowed us to test cytoadhesion in Petri dishes coated with CSA or BSA as a control. Upon deletion of FIKK4.1, a 55% reduction in cytoadhesion was observed relative to the DMSO control (mean reduction in cytoadhesion = 55.01±1.94%; mean±SEM; n=5) (Figure 5E). No significant differences were observed for RAP-treated NF54 or FIKK10.2.

As the major knob component KAHRP is differentially phosphorylated upon FIKK4.1 deletion, it was hypothesised that the reduction in cytoadhesion may be a result of a defect in knob formation. However,

scanning electron microscopy (SEM) did not reveal any obvious abnormality in knobs between DMSO and RAP-treated FIKK4.1 cKO parasites (Figure S4D). Likewise, negative stain electron tomography [41] on RBC ghosts did not reveal any differences in the size, shape, distribution, or structural features of knobs between RBCs infected with RAP-treated FIKK4.1 cKO parasites compared to 3D7 wildtype parasites (Figure 5F and Figure S4E), suggesting that FIKK4.1 does not play a role in knob architecture. This indicated that PfEMP1 trafficking to the surface may be affected. Quantification of surface exposed VAR2CSA by flow cytometry revealed a 46.7% reduction in the median fluorescence intensity observed in RAP-treated FIKK4.1, but not in NF54::DiCre or FIKK10.2 parasite lines (mean reduction = 46.7±3.04%; mean±SEM; n=4) (Figure 5G, 5H). As PfEMP1 was still observed to some extent on the surface of most iRBCs, it is likely that a reduction in avidity due to fewer PfEMP1-CSA interactions is responsible for the cytoadhesion defect upon FIKK4.1 deletion.

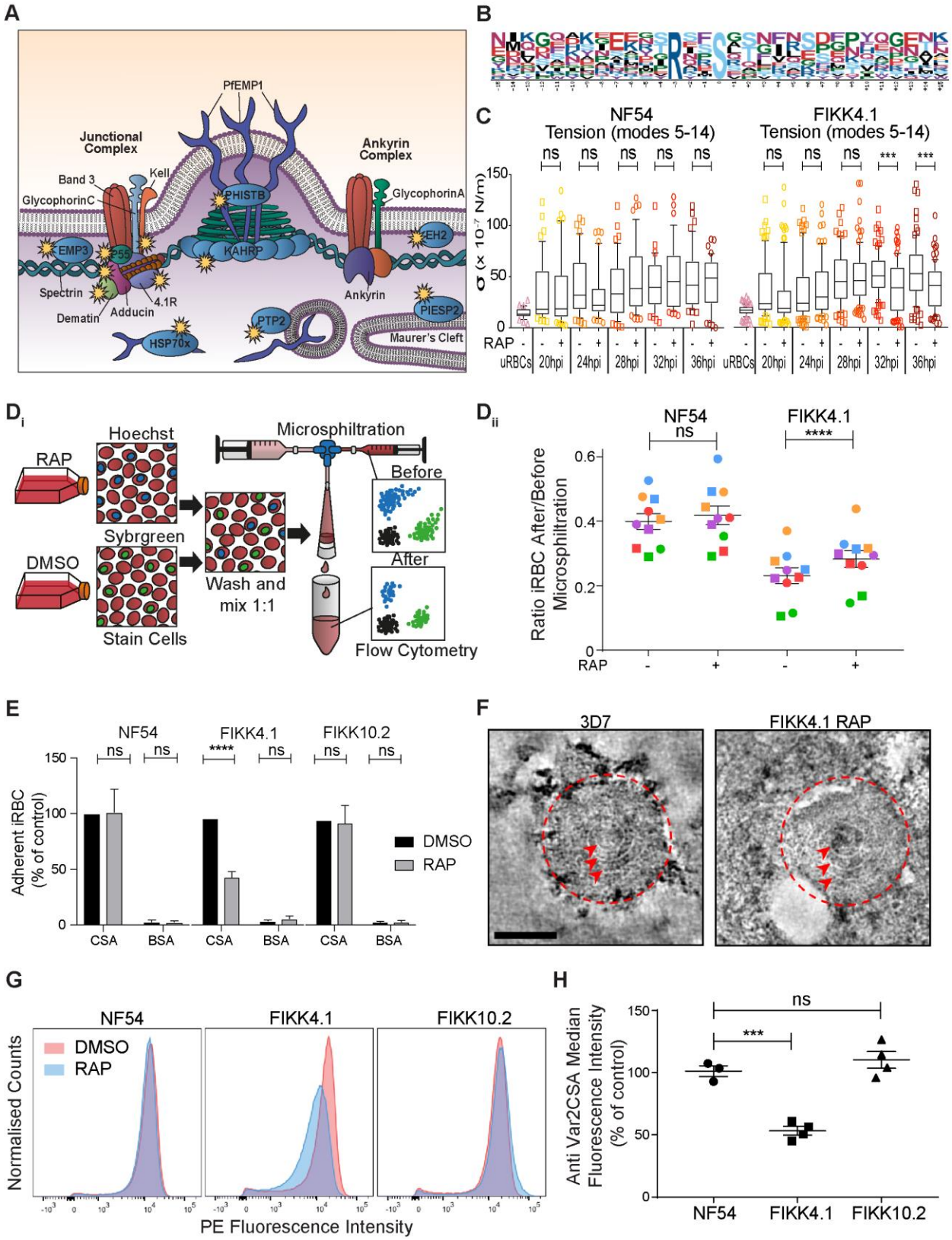

Figure 5: FIKK4.1 is important for modulation iRBC rigidity and PfEMP1 surface translocation
(A) Graphical representation of FIKK4.1 substrates identified by mass spectrometry (depicted with ✸). The representation focuses on the knob structures. **(B)** Arginine-based phosphorylation motif identified on FIKK4.1 substrates. See also Table S4. **(C)** Time-course flicker spectroscopy comparing the membrane

tension of uRBCs, NF54::DiCre and FIKK4.1 cKO iRBCs, DMSO or RAP-treated. Horizontal lines within boxes represent the median and the whisker boundaries represent the 10th and 90th percentile (*** p<0.001). **(D_i)** Diagram illustrating the microsphiltration experiment. **(D_{ii})** Ratio of iRBCs after and before microphiltration. Each point is an individual measurement with technical replicates from the same experiment represented in the same colours. Error bars show mean±SEM, n = 10 (**** p<0.0001 for paired multiple comparison ANOVA). **(E)** Percentage of iRBCs bound to CSA compared to the positive control (DMSO-treated parasites on CSA). Shown is the mean cytoadhesion compared to control±SEM, n = 5 (**** p<0.0001). **(F)** SEM images of the surface of erythrocytes infected with DMSO or RAP-treated FIKK4.1::DiCre parasites (scale bar = 1µm). **(G)** Typical knob complexes from wild-type 3D7 and FIKK4.1 KO schizonts imaged by negative stain electron tomography. The knob coat is outlined with a red dashed line and the underlying knob spiral is indicated by red arrowheads. Side views of the knobs are also available in Figure S4E. Images are an average of 5 central slices of the tomogram (scale bar = 50 nm). **(H)** Quantification of the VAR2CSA median fluorescence intensity in RAP-treated parasites compared to the control (DMSO-treated)±SEM, n = 4 (*** p<0.001). See also Figure S4.

Discussion

Through extensive phosphoproteomic profiling we have identified species-specific effectors of the most pathogenic human malaria parasites and established their role in regulating virulence traits. While it was previously established that RBC proteins are phosphorylated upon *P. falciparum* infection [31,42], the scale of this change has exceeded previous estimates and suggests that the RBC is being actively manipulated by the parasite. Species-specific RBC phosphosites are observed on proteins predicted to play a role in cytoskeletal connections, nutrient permeability, and the ubiquitination system, all of which have been previously reported to be modulated during *P. falciparum* infection [43-47]. Interestingly, some of the FIKK-dependent RBC phosphosites we identified were shown to be important for parasite invasion [48,49]. Our data indicates that the FIKK kinases may be responsible for co-opting these host components to the advantage of the parasite.

The vital role of FIKK4.1 in PfEMP1-mediated adhesion to CSA suggests that expansion of the FIKK kinases facilitated the evolution of *Laverania*-specific changes to the RBC [14]. Phosphorylation of PfEMP1 trafficking proteins was dependent on a number of other FIKKs in addition to FIKK4.1, suggesting that several kinases may be important to this pathway. As well as lacking PfEMP1, other human-infecting *Plasmodium* species do not form knobs on the cell surface. While we observed no striking differences in knob formation upon deletion of FIKK4.1, deletion of FIKK4.2 has been previously shown to affect knob morphology [21]. Here we show that FIKK4.2 controls phosphorylation of the knob protein KAHRP and the lysine-rich membrane-associated PHISTb protein (LYMP) which binds PfEMP1, providing a possible molecular mechanism for this phenotype [8,9]. Several FIKKs may act together to support the surface display of PfEMP1.

The unique phosphorylation fingerprint of each FIKK kinase suggests that while some FIKKs may operate in the same pathways, each has an independent role. The specificity of the FIKKs is likely due to their differing expression patterns, their localisation within the cell, and their substrate specificities. FIKK4.1 showed a preference for the R/KxxS/T phosphorylation motif and FIKK8 preferentially phosphorylates this motif *in vitro* [20]. FIKK1 appears to localise to Maurer's clefts by immunofluorescence, however its phosphorylation of a cytoskeletal protein suggests it may be able to move between these sites. The localisation of FIKK4.1 and FIKK4.2 at the RBC periphery is likely due to the basic repeats at their N-termini, as observed for similar sequences in other exported proteins [50].

Although no growth defect was observed upon deletion of any exported FIKK kinase under optimal cell culture conditions, FIKK9.3 has been previously implicated in providing some protection against elevated temperatures, suggesting FIKKs may be important for survival within the host [51]. Some FIKKs may also be important in other life stages; RBC rigidity and morphology are both important for the sequestration of *P. falciparum* gametocytes in the bone marrow during maturation, which is also unique to *Laverania* parasites [52-54]. As all cKO lines were made in an NF54::Dicre line capable of transmitting through mosquitoes, it will be possible to test their roles at all life stages in the future.

As we demonstrate for FIKK4.1, knowing the substrates of these FIKKs can provide a mechanistic understanding of species-specific disease outcomes. By blocking the activity of multiple FIKK kinases simultaneously using kinase inhibitors, it may be possible to prevent RBC remodelling entirely to ease disease symptoms and enable rapid clearance of infected cells by the host immune system.

Material and Methods

Phylogeny

The protein sequences of FIKK8 orthologues from all available *Plasmodium* species were downloaded from PlasmoDB. Multiple sequence alignment was performed with ClustalW [55], then maximum likelihood-based phylogeny was calculated by PhyML [56]. The phylogenic tree was visualized with FigTree v1.4.4 [57] using a radial tree layout with branches transformed to equal length for clarity.

In vitro maintenance and synchronization of parasites

Asexual RBC stage *P. falciparum* parasites were cultured at 37°C in complete media (CM). Complete media consists of RPMI-1640 medium which was supplemented with 5g Albumax II (ThermoFischer Scientific) to act as a serum substitute, 0.292g L-glutamine, 0.05g hypoxanthine, 2.3g sodium bicarbonate, 0.025g gentamicin, 5.957g HEPES and 4g dextrose. Parasites were grown at 1-5% haematocrit; blood was from anonymous donors, provided through the UK Blood and Transfusion service. Parasites were grown in a parasite gas atmosphere (90% N_2, 5% CO_2, 5%O_2) [58]. Parasite growth was routinely examined by Giemsa staining of methanol-fixed air-dried thin blood smears followed by visualisation by light microscopy. Asexual RBC stage *P. knowlesi* parasites were cultured in CM supplemented with 10% human serum as described previously [24]. Parasite cultures were synchronised by isolating mature schizont-stage parasites on a cushion of 60% Percoll (GE Healthcare). Purified schizonts were incubated in CM at 37°C with fresh RBCs for 1-4 hours in a shaking incubator. Any remaining schizonts were removed by a second Percoll purification to leave tightly synchronised ring-stage parasites.

Magnetic Purification

Components for the magnet rack were designed using Autodesk Inventor software and printed with an Objet30 3D printer using VeroGray resin. Strong 1-inch neodymium magnets (K&J magnetics) were inserted into the rack, which was sealed with tape. The rack is assembled by inserting the T-shaped tabs into the legs to position the tube rack and the magnet-holder. CS-MACS (Miltenyi Biotec) columns are filled with RPMI from a 2-way stopcock then inserted into the magnet-holder. Columns were washed with 10mL RPMI before use, then attached to 23 gauge blunt-ended syringe filters to control flow speed. The RBC suspension was added to the column at a hematocrit of under 20%, then washed with RPMI. Once the flowthrough ran clear, the columns were washed with an additional 20mL of RPMI. The columns were

removed from the magnet and placed in 15mL tubes, and late-stage iRBCs were eluted with 10mL of RMPI, with the syringe tips still attached. Purity of both the elution and the flowthrough were checked by giemsa smear. If parasitemia in the elution was under 95%, the columns were returned to the magnet-holder and the eluate passed through one more time, with 10mL RPMI for washing, before a final elution with 10mL RPMI. Columns were washed with 100mL H2O followed by 10mL 70% EtOH, then dried and stored in a 37°C incubator.

Mass spectrometry

Cell culture, lysis and protein digestion - across all experiments, iRBCs were enriched by magnet purification at 40-46hpi for *P. falciparum* iRBCs and ~24hpi for *P. knowlesi* iRBCs, to a purity of between 95-99% parasitemia. Flowthrough uRBC samples contained <1% infected cells. Samples were immediately lysed in ice cold 8M urea in 50mM HEPES pH8.5, supplemented with protease (complete mini, Roche) and phosphatase (Phos Stop, Roche) inhibitors, and snap frozen in liquid nitrogen for storage at -80°C. Once thawed, samples were further solubilized by sonication (30% duty cycle, 3 x 30 seconds bursts, on ice). Protein concentration was then calculated using a BCA protein assay kit (Pierce), first diluting 50uL sample aliquots from all lysates 1:3 in 50mM ammonium bicarbonate to reduce the concentration of urea, and then following the instructions included in the kit. Lysates (1 mg each) were subsequently reduced with 5mM DTT for 30 minutes at 56°C and alkylated in the dark with 14mM iodoacetamide for 30 minutes at RT. Following iodoacetamide quenching with 5mM DTT for 15 minutes in the dark, lysates were diluted with 50mM ammonium bicarbonate to < 4M urea, and digested with LysC (Promega) for 2-3 hours at 37°C. Lysates were further diluted with 50mM ammonium bicarbonate to < 2M urea and digested with trypsin (Promega) at 1:50 (enzyme:protein) overnight at 37°C.

Sep-Pak desalting - samples were acidified with trifluoroacetic acid (TFA) (Thermo Fisher Scientific) to a final concentration of 0.4% (v/v) and left on ice for 10 minutes. All insoluble material was removed by centrifugation (4000 rpm, 10 minutes, 4°C) and supernatants were desalted on Sep-Pak lite C18 cartridges (Waters) in conjunction with a vacuum manifold. Columns were first washed with 3mL acetonitrile, conditioned with 1mL of 50% acetonitrile, 0.5% acetic acid in H2O, then equilibrated with 3mL of 0.1% TFA in H2O. The acidified samples were loaded, then desalted with 3mL of 0.1% TFA in H2O, washed with 1mL of 0.5% acetic acid in H2O then finally eluted with 1.2mL of 50% acetonitrile, 0.5% acetic acid in H2O. Each sample was then dried by vacuum centrifugation.

TMT labelling – Samples were dissolved at 1 mg/mL in 50mM Na-Hepes, pH 8.5 and 30% acetonitrile (v/v) and labelled with respective TMT reagents (Thermo Fisher Scientific, 2.5mg reagent/1mg sample) for 1 hour at RT. Labelling was then quenched with 0.3% hydroxylamine for 15 minutes at RT and samples acidified (pH~2) with formic acid. Subsequently, 2 µL aliquots of each labelled sample were mixed in 200 µL of 1% formic acid, stage tipped (see the Stage tip section below), and a test LC-MS/MS run was performed on a Q-Exactive mass spectrometer (see the LC-MS/MS section below) to verify labelling efficiency. If the reporter intensity ratios between samples were < 1.5, the lysates were mixed in a 1:1 ratio, vacuum dried and desalted on Sep-Pak C18 cartridges (2 columns/10mg protein) as described above.

Strong cation exchange (SCX) fractionation – for experiments 1, 2 and 3 SCX fractionation was performed prior to phosphopeptide enrichment. Peptides were resuspended in 400µL of 10mM ammonium formate pH 3, 25% acetonitrile by sonication and all insoluble material was removed by centrifugation. Samples were loaded on a 20 cm Polysulfoethyl-A column (4.6 mm inner diameter, 5 µm particle size, PolyLC) and fractionated using Agilent 1200 (Agilent) HPLC with a binary buffer system (solvent A: 10 mM ammonium formate pH 3, 25% acetonitrile; solvent B: 500mM ammonium formate pH 6.8, 25% acetonitrile) at a flow rate of 0.8mL/minute. The samples were run on a linear gradient of 0-60% B in 20 minutes and 60-100%B in 5 minutes with a total run time of 40 minutes including column conditioning. A total of 12 fractions were collected and vacuum dried.

Phosphopeptide enrichment – samples were solubilized in 1mL of loading buffer (80% acetonitrile, 5% TFA, 1M glycolic acid) and mixed with 5mg of TiO2 beads (Titansphere, 5 µm GL Sciences Japan). Samples were incubated for 10 minutes with agitation, followed by a 1 minute 2000 × g spin to pellet the beads. The supernatant was removed and used for a second round of enrichment as explained below. Beads were washed with 150µL of loading buffer followed by two additional washes, the first with 150µL 80% acetonitrile, 1% TFA and the second with 150µL 10% acetonitrile, 0.2% TFA. After each wash, beads were pelleted by centrifugation (1 minute at 2000 × g) and the supernatant discarded. Beads were dried in a vacuum centrifuge for 30 minutes followed by two elution steps at high pH. For the first elution step, beads were mixed with 100µL of 1% ammonium hydroxide (v/v) and for the second elution step with 100µL of 5% ammonium hydroxide (v/v). Each time beads were incubated for 10 minutes with agitation and pelleted at 2000 × g for 1 minute. The two elutions were removed following each spin, and subsequently pooled together before undergoing vacuum drying.

The supernatant from the TiO2 enrichment was desalted on two Sep-Pak columns and the High Select Fe-NTA phosphopeptide enrichment kit (Thermo Fisher Scientific) was used according to manufacturer's instructions for a second round of enrichment. The supernatant containing all non-phosphorylated peptides (total proteome) was removed and stored at -80°C.

High pH sample fractionation – for experiments 4, 5 and 6 combined TiO2 and Fe-NTA phosphopeptide eluates were fractionated using the Pierce High pH Reversed-Phase kit (Thermo Fisher Scientific) according to manufacturer's instructions.

Stage tip desalting – all samples were desalted prior to LC-MS/MS using Empore C18 discs (3M). Briefly, each stage tip was packed with one C18 disc, conditioned with 100µL of 100% methanol, followed by 200µL of 1% TFA. The sample was loaded in 100µL of 1% TFA, washed 3 times with 200µL of 1% TFA and eluted with 50µL of 50% acetonitrile, 5% TFA. The desalted peptides were vacuum dried in preparation for LC-MS/MS analysis.

LC-MS/MS and data processing – Samples were resuspended in 0.1% TFA and loaded on a 50 cm Easy Spray PepMap column (75 µm inner diameter, 2 µm particle size, Thermo Fisher Scientific) equipped with an integrated electrospray emitter. Reverse phase chromatography was performed using the RSLC nano U3000 (Thermo Fisher Scientific) with a binary buffer system (solvent A: 0.1% formic acid, 5% DMSO; solvent B: 80% acetonitrile, 0.1% formic acid, 5% DMSO) at a flow rate of 250 nL/minute. The samples were run on a linear gradient of 5-60% B in 150 minutes (Lumos) or 2-35% in 155 minutes (Q-Exactive) with a total run time of 180 minutes including column conditioning. The nanoLC was coupled to mass spectrometers using an EasySpray nano source (Thermo Fisher Scientific). The Orbitrap Lumos was operated in data-dependent mode. For the MS2 method, HCD MS/MS scans (R=50,000) were acquired after an MS1 survey scan (R=120, 000) using MS1 target of 4E5 ions, and MS2 target of 2E5 ions. The number of precursor ions selected for fragmentation was determined by the "Top Speed" acquisition algorithm with a cycle time of 3 seconds, and a dynamic exclusion of 60 seconds. The maximum ion injection time utilized for MS2 scans was 86 ms and the HCD collision energy was set at 38. For the MS3 method, CID MS/MS scans (R=30,000) were acquired after an MS1 survey scan with parameters as above. The MS2 ion target was set at 5E4 with multistage activation of the neutral loss (H3PO4) enabled. The maximum ion injection time utilized for MS2 scans was 80 ms and the CID collision energy was set at 35. HCD MS3 scan (R=60,000) was performed with synchronous precursor selection enabled to include up to 5 MS2 fragment ions. The ion target was 1E5, maximum ion injection time was 105 ms and the HCD

collision energy was set at 65. The Q-Exactive was operated in data-dependent mode acquiring HCD MS/MS scans (R=35,000) after an MS1 survey scan (R=70, 000) on the 10 most abundant ions using MS1 target of 1E6 ions, and MS2 target of 2E5 ions. The maximum ion injection time utilized for MS2 scans was 120 ms, the HCD normalized collision energy was set at 33 and the dynamic exclusion was set at 30 seconds. The peptide match and isotope exclusion functions were enabled.

Acquired raw data files were processed with MaxQuant [59] (version 1.5.2.8) and peptides were identified from the MS/MS spectra searched against *Plasmodium falciparum*, *Plasmodium knowlesi* (PlasmoDB, 2018) and *Homo sapiens* (UniProt, 2018) proteomes using Andromeda [60] search engine. TMT based experiments in MaxQuant were performed using the 'reporter ion MS2 or MS3' built-in quantification algorithm with reporter mass tolerance set to 0.003 Da. Cysteine carbamidomethylation was selected as a fixed modification. Methionine oxidation, acetylation of protein N-terminus, deamidation (NQ) and phosphorylation (S, T, Y) were selected as variable modifications. The enzyme specificity was set to trypsin with a maximum of 2 or 3 missed cleavages depending on the experiment. The precursor mass tolerance was set to 20 ppm for the first search (used for mass re-calibration) and to 4.5 ppm for the main search. 'Match between runs' option was enabled (time window 0.7 min) for fractionated samples. The datasets were filtered on posterior error probability (PEP) to achieve a 1% false discovery rate on protein, peptide and site level.

Data analysis

Mass spectrometry data sets were first input into Perseus [61] for annotation of protein names and the organism or origin. The data were filtered to remove common contaminants and IDs originating from reverse decoy sequences. To generate a list of all quantified phosphosites reporter intensities were filtered for 1 valid value. Subsequent data analysis was done using R programing in R studio. General-usage R packages used were readxl, xlsx, matrixStats, gridExtra, ggplot2, matrixStats, gplots, and svglite.

The TMT label intensity values were log2 transformed for each experiment. The data were normalized by median ratio normalization, which is used for library size normalization of RNA-seq datasets using the R package DeSeq2 [62]. Briefly, the mean log2 intensities were calculated for each phosphopeptide where values were observed across all ten samples in a given experimental run (mean of each row). This row mean was then subtracted from each original log2 intensity in a given row. A median was taken of each column of this data to get a scaling factor for each sample, which was then subtracted from the original

log2 intensities in a given column to get the normalized intensities. For experiment 1, phosphosites from Human, *P. falciparum*, and *P. knowlesi* proteins were normalized using a scaling factor calculated from Human RBC phosphosites only, as this was assumed to remain approximately constant for each sample. For experiments 2, 3, 4, 5, and 6, the scaling factor was calculated individually for Human and *P. falciparum* phosphosites, to account for any differences in the purity of iRBC between samples.

For experiment 1, the TMT label intensities for each sample were averaged across replicates and Log2 Fold Change values were calculated by pairwise comparisons of Human phosphosites between *P. falciparum* and *P. knowlesi* iRBCs, between *P. falciparum* iRBCs and uRBCs, and between *P. knowlesi* iRBCs and uRBCs. Log2 fold change values and -Log10 *P*-values (Welch's pairwise t-tests) were calculated individually for each of the three mass spectrometry runs, then averaged. Phosphosites were considered significantly changing if they exceeded a non-linear threshold based on the log2 fold change values and the *P*-values. The threshold was defined as:

$$y = \frac{c}{|x| - x_0}$$

Where:

y: -log10 *P*-value

x: log2Fold Change

x0: log2Fold change threshold (set to 1.5)

c: curvature constant (set to 1.5)

A discordance (DISCO) plot of *P. knowlesi* iRBCs and *P. falciparum* iRBCs was plotted with the log2 fold changes of PK iRBCs-uRBCs against PF iRBCs-uRBCs. DISCO scores for each phosphosite were calculated using [63]:

$$DISCOscore = (log2FC\ PF - log2FC\ PK) \times (-log10Pvalue\ PF + -log10Pvalue\ PK)$$

For experiment 2, we investigated the effect of different donors and blood type on phosphorylation within the RBC. A one-way ANOVA test was performed in R on human phosphosites across both uninfected and infected samples. Additional ANOVA tests were performed and correlation coefficients calculated to test for differences between blood types in the phosphorylation of uRBC proteins, the log2 fold change in RBC

proteins between uRBCs and *P. falciparum* iRBCs, and the phosphorylation of *P. falciparum* proteins. Correlation plots are also shown for each comparison (Figure S1).

For experiments 3,4,5, and 6, Log2 fold change values were calculated between DMSO and RAP-treated samples within each experiment, then averaged between the replicates for FIKK1, FIKK4.1, FIKK4.2, FIKK10.2, and FIKK11 cKO lines. The significance threshold was set at 4* standard deviation of the Log2 fold change values for a given FIKK kinase. For experiment 4 and 5, the Log2 fold change between the NF54 parental line and the *P. knowlesi* iRBC line was also calculated for Human proteins only. Violin plots were created using the R package ggplots2. Proteins were annotated as exported if they have an exportpred score > 1 (PlasmoDB), or are annotated with Go-component terms which contained the words 'host cell' or 'maurer's cleft'. The heatmap.2 function from the R package gplots was used to create heatmaps which included all sites which were observed across experiments 3, 4, 5, and 6, and which were phosphorylated less upon deletion of at least one FIKK kinase as these are likely to be true substrates. Sites (rows) are clustered by the complete linkage method with Euclidean distance measure.

Plasmids and Parasite Transfection

Plasmids for the cKO lines were constructed as described previously [27] with some changes. Recodonised kinase domains with loxP introns were initially purchased from IDT as 'custom genes' inserted into a plasmid for FIKK4.1, FIKK7.1, FIKK8, FIKK10.1, and FIKK11. Subsequently, recodonised kinase domains fused to 3x HA but without the loxP introns were ordered as gblocks from IDT (Table S5). For cKO lines integrated using selection-linked integration (All FIKKs apart from FIKK9s, FIKK12 and FIKK10.1 in NF54), the 5' homology arm, loxP intron, and the recodonised kinase domain with HA tag were PCR-amplified from *P. falciparum* NF54 genomic DNA, IDT 'custom genes', or IDT gblocks, respectively. Fragments were inserted by Gibson assembly into a previously-made pARL-based plasmid containing the T2A skip peptide, neomycin resistance cassette, second loxP intron, and GFP, which was digested at BglII and SalI restriction sites. The plasmid also contained a WR resistance cassette (for selection in the parasite) and an Ampicillin resistance cassette (for selection in *E. coli*). 100ug of the plasmid was obtained by midiprep from *E. coli* top 10 cells and transfected into highly synchronized 48hpi schizonts (either 1G5 or NF54) using an Amaxa electroporator and Lonza 4D-Nucleofector kit with P3 Primary cell buffer. Transfected lines were drug-selected after 48 hours, first with 2.5 nM WR99210 (Jacobus Pharmaceuticals) until iRBCs were visible by

giemsa smear, then with 225µg/ml G418 (Gibco by LifeTechnology) to ensure correct integration into the FIKK locus.

For single FIKK cKO lines integrated by CrispR/Cas9, the rescue plasmid was constructed by PCR amplifying the 5' homology region, loxP intron, recodonised kinase domain-3xHA, T2A-neomycin-loxPintron-GFP sequence, and 3' homology region, then using Gibson assembly to insert all fragments into a pMK-RQ plasmid (IDT) containing a Kanamycin resistance cassette. 60 ug of this plasmid was digested by EcoRI, which was then heat-denatured at 65°C for 30 minutes. The digested plasmid was then combined with 20ug of a PDC2 plasmid containing Cas9 under a CAM promoter, the tracR RNA under a U6 promoter, and a hDHFRuFCU resistance cassette for positive selection with WR and negative selection by ancotil. The guide RNA sequence was inserted into bbsII cleavage sites in the tracR RNA sequence by Gibson assembly. Schizonts were transfected as described above and selected after 24h with 2.5 nM WR99210, which was added daily for 4 days. Once iRBCs were visible by giemsa smear, iRBCs were further selected with 225µg/ml G418.

For the FIKK9.1-FIKK9.7 deletion, a 9-fragment Gibson assembly was performed to create the rescue plasmid. This combined the FIKK9.1 5' homology region, recodonised FIKK9.1-3xHA tag- loxP intron-T2A sequence (ordered from Geneart, see table S5), Neomycin cassette, FIKK9.1 3' homology region, FIKK9.7 5' homology region, recodonised FIKK9.7-loxP sequence (ordered from Geneart), FIKK9.5 3' homology arm, and a pMK-RQ plasmid (IDT), which was digested by HindIII and NcoI. 60ug of the plasmid was digested by EcoRI. The Crispr/Cas9 plasmid contained guides against both FIKK9.1 and FIKK9.7, which were first inserted individually into the cas9 plasmid as described above. The U6 promoter, tracR RNA and FIKK9.1 guide were then PCR amplified and inserted by Gibson assembly into the SalI site of the plasmid containing the FIKK9.7 guide RNA. 20ug of this plasmid was combined with the 60ug of digested rescue plasmid, and transfected into purified schizonts. Transfected parasites were selected after 24h with 2.5 nM WR99210 for 4 days.

Correct integration of all transfectants was confirmed by PCR (see table S5 for primers). Parasite lines were cloned as described [30]. The concentration of iRBCs was calculated and diluted into a suspension of complete media at 0.75% hematocrit, to approximately 500 parasites/mL. A 3-fold serial dilution series was dispensed into the wells, from 100 to 0.1 parasites per well in 200uL. After between 10-14 days, plaques per well were counted, and any wells containing a single plaque were transferred to round-bottomed 96-well plates and supplemented with fresh blood to 2% hematocrit. After approximately 14 days, the wells

were checked by giemsa smear and samples from parasite-positive wells were then taken for PCR analysis to check for correct integration of the plasmids. 4 wells containing the desired insertion were transferred to T25 flasks, and one clone was then selected for all further experiments. For all experiments, ring-stage parasites were treated with either 100nM Rapamycin or DMSO for 4 hours, and excision was confirmed by PCR (figure S2).

Plaque assay assessment of parasite growth

Parasite lines were tightly synchronized to a 4-hours window using Percoll (GE Healthcare). Synchronous parasite cultures at ring stage were treated with either DMSO or Rapamycin followed by 3 washes with Complete Medium (CM). Plaque assays were performed as previously described by Thomas *et al.* [30]. DMSO- and RAP-treated parasites were plated in the same flat-bottomed 96-well plates (Corning 3596) using the central 60 wells of the plate, 30 for DMSO- and 30 for RAP-treated culture (10 parasites per well, 200µL CM, 0.75% Haematocrit). Evaporation was limited by adding sterile PBS to the outer wells. Plates were incubated in gassed chamber (C.B.S Scientific Culture Chamber M-312) filled with parasite gas (90% N2, 5% CO2, 5% O2) for 12 days. Plates were imaged using a Perfection V750 scanner (Epson) in top-down transmission light mode, saving images as 4,800dpi TIFF files. Wells of interest were selected using the Magic Wand tool (tolerance setting = 75) of Adobe Photoshop CC 2018. Finally, number of plaque and plaque area for each well were quantified using the Analysing Particles tool in Fiji (Size = 10-750 pixels; Circularity = 0.2-1.00). PRISM8 (GraphPad) was used for statistical analysis of plaque assay data by unpaired *t*-test. A *P*-value of <0.05 was considered statistically significant.

FACS analysis of parasite growth

For parasitemia measurements by flow cytometry, parasites were tightly synchronised to a 4-hour window by Percoll synchronisation. Immediately after synchronisation, ring stage parasites were treated for 4 hours with either DMSO or RAP followed by 3 washes with CM. NF54 cultures were then adjusted to 1% parasitemia 5% haematocrit in 5ml CM in triplicate wells of six-wells plates (ThermoScientific 140675) and incubated in a gassed chamber (C.B.S Scientific Culture Chamber M-312) filled with parasite gas (90% N2, 5% CO2, 5% O2). Every 24 hours, DMSO- and RAP- treated parasites from 2 different wells each day were fixed in 2% paraformaldehyde/0.2% glutaraldehyde in PBS. 1G5 cultures were adjusted to 0.1% parasitemia, 5% haematocrit in 10ml CM in T25 flasks and samples were fixed same as above every 12

hours. Fixative was washed out with PBS and samples were stained with Hoechst 33342 (NEB) diluted 1:2000 in PBS for 15 minutes in the dark at 37°C. After a final wash, Hoechst-positive cells were counted by flow cytometry on a BD LSRFortessa flow cytometer (Becton Dickinson). Data were analysed using FlowJo10 analysis software (Becton Dickinson).

Immunoprecipitation and Western blot

FIKK7.1 HA-expressing parasites were lysed in 5ml RIPA buffer (ThermoFischer Scientific) by incubation on ice for 20-30 minutes. 100µl of anti-HA affinity matrix (Sigma-Aldrich) per condition was washed 3 times in RIPA buffer. 1ml of parasite lysate was spun at 13000rpm for 30 minutes at 4°C. Supernatants from lysates were mixed together with washed anti-HA affinity matrices and left to incubate at 4°C for 2-3 hours on a rotating wheel. Matrices were washed 3 times in RIPA buffer, boiled for 10 minutes in protein loading buffer and bound proteins were recovered in the supernatant after centrifugation.

All other western blot samples were obtained from Percoll-enriched schizonts resuspended in PBS, solubilised in protein loading buffer and denatured at 95°C for 10 minutes.

Parasite extracts and immunoprecipitation samples were subjected to SDS-PAGE, transferred to Transblot® Turbo™ Mini-size nitrocellulose membranes (BIORAD) and blocked overnight in 5% skimmed milk in PBS/0.2%Tween-20 at 4°C. For integration and excision checks (Figure 2C), membranes were probed with rat anti-HA high affinity antibodies (Roche (1:1000)) and rabbit anti-MAHRP1 antibodies (1:2000) followed by incubation with relevant secondary fluorochrome-conjugated antibodies (Donkey anti-rabbit IRDye 680LT (LI-COR) (1:20000); Goat anti-rat IRDye 800CW (LI-COR) (1:20000)). For western blots investigating adducin S726 phosphorylation (Figure 3E), membranes were probed with rat anti-HA high affinity antibodies (Roche (1:1000)), rabbit anti-MAHRP1 (1:2000), B-12 mouse anti-spectrin (SantaCruz Biotechnology (1:10000)), rabbit anti-dematin (Invitrogen (1:1000)), mouse anti-αadducin (Abcam (1:2000)) and rabbit anti-αadducin p726 (Abcam (1:1500)). The same secondary fluorochrome-conjugated antibodies were used as above in addition to goat anti-mouse IRDye 680LT or 800CW (LI-COR) (1:20000).

Antibody reactions were carried out in 5% skimmed milk in PBS/0.2%Tween-20 and washed in PBS/0.2%Tween-20. Antigen-antibody reactions were visualized using the Odyssey Infrared Imaging system (LI-COR Biosciences, Nebraska, United States).

Immunofluorescence assay

22x22mm coverslips (VWR International) were coated with 200µl of Concanavalin A (Santa Cruz Biotechnology, 5mg/ml in water) for 20 minutes in a humid chamber at 37°C. In the meantime, iRBCs from culture were rinsed twice with 1ml of pre-warmed PBS by centrifugation in at 2000rpm for 2 minutes and diluted to 1% haematocrit still in pre-warmed PBS. Coverslips were washed with 200µl of pre-warmed PBS and 200µl of the 1% haematocrit solution was added onto the coverslips. After 15 minutes incubation at 37°C, unbound cells were gently washed away with PBS and remaining cells were fixed with freshly made 2% paraformaldehyde in PBS for 20 minutes at room temperature. The fixative was removed and fixed cells were rinsed 3 times with PBS. Cells were permeabilised with 0.1% Triton® X-100 diluted in PBS for 20 minutes followed by 3 washes with PBS. Cells were blocked with 3% BSA in PBS for 1 hour at room temperature. Labelling of the cells was performed for at least 1 hour at room temperature with primary antibody diluted in PBS 1% BSA: high affinity anti-HA (Roche) (1:1000); anti-MAHRP1 (1:1000) (gift from Julian Rayner); anti-PTP2 (1:250) (gift from Alan Cowman) [37]; anti-Hsp70-x (1:200) (gift from Jude Przyborski) [64]. After 3 washes with PBS, coverslips were incubated with relevant Alexa Fluor secondary antibodies (1:2000 in PBS 1% BSA) at room temperature for 1 hour, in the dark. After 3 final washes with PBS, coverslips were mounted in Prolong® Gold antifade reagent (Invitrogen) containing the DNA dye 4', 6-diamidino-2-phenylindole (DAPI) and sealed with nail polish. Images were taken using a Ti-E Nikon microscope using a 100x TIRF objective at room temperature equipped with a LED-illumination and an Orca-Flash4 camera. Images were processed with Nikon Elements software (Nikon, Japan).

Network

An undirected network was constructed in Cytoscape [65] with the 13 FIKK kinases as the main nodes connected to other nodes that represent RBC and exported *P. falciparum* phosphoproteins. Betweenness centrality of each node was calculated and the network was shown in a force-directed layout with some manual arrangement, with nodes with degree of 1, i.e. proteins that only connect to one FIKK kinase, removed. The thickness of the connecting line represents the number of sites significantly changing on each protein due to each kinase, while lines are coloured according to the average log2 fold change of all the significantly-changing sites. Symbol size represents the number of connections (degree) to each protein.

Motif-x

All phosphorylation sites identified to be dependent for a given FIKK were analyzed for a specific phosphorylation motif using rmotif-x [66] using the standard parameters. All phosphorylation sites identified in all experiments were set as background and phosphorylation sites that were reduced in phosphorylation state upon FIKK deletion were used as the foreground dataset.

Membrane contour detection and flickering spectrometry

Plasmodium falciparum NF54 and FIKK 4.1 parasite cultures treated with DMSO and treated with RAP were synchronised to a one hour window by Percoll (GE Healthcare) before imaging. Then parasites were diluted in culture medium (RPMI-1640 supplemented with HEPES, 40 mM; D-glucose, 10 mM; glutamine, 2 mM; gentamicin sulphate, 25 mg/L; AlbumaxII, 0.5 % vol/vol) (Sigma) at 0.01% haematocrit and transferred in SecureSeal Hybridization Chambers (Sigma-Aldrich). A custom-built temperature control system was used to maintain the optimal culture temperature of 37°C during imaging experiments. The sample was placed in contact with a transparent glass heater driven by a PID temperature controller in a feedback loop with the thermocouple attached to the glass slide. A Nikon Eclipse Ti-E inverted microscope (Tokyo, Japan) was used with a Nikon 60X Plan Apo VC, N.A. 1.40, oil immersion objective, kept at physiological temperature through a heated collar. Motorized functions of the microscope were controlled via custom software written in-house. Videos were acquired for around 20 seconds in bright field using a CMOS camera (model GS3-U3-23S6M-C, Point Grey Research/FLIR Integrated Imaging Solutions (Machine Vision), Ri Inc., Canada) at 514 frames/s and 0.8 ms exposure time. 50 parasites for each condition (NF54 + DMSO, NF54 + RAP, FIKK 4.1 + DMSO, FIKK 4.1 + RAP) were recorded at 20, 24, 28, 32, and 36 hours post invasion by two experimentalists using two microscopes at the same time. Recordings of uninfected erythrocytes were also taken in the same period of time. Data from two biological replicates were analysed.

To obtain biophysical parameters such as bending modulus, tension, radius, and viscosity of cells, we employed the flickering spectroscopy technique. First, erythrocyte contours were detected for each frame with subpixel resolution by an optimised algorithm developed in house and implemented in Matlab (The MathWorks, Natick, MA). Contour detection of infected erythrocytes after 36 hours was difficult due to the uneven, non-uniform equatorial shape of the cells caused by the development of the parasite inside. Detailed explanations of the contour detection algorithm and the membrane fluctuation analysis are

extensively described in previous works [38,67,68]. Briefly, the contour was decomposed into fluctuation modes by Fourier transform to give a fluctuation power spectrum of mean square mode amplitudes at the cell equator $\langle|h(q_x, y=0)|^2\rangle$ as a function of mode wave vector q_x. The bending modulus κ and tension σ can then be fitted using the following equation:

$$\langle|h(q_x, y=0)|^2\rangle = \frac{1}{L}\frac{k_B T}{2\sigma}\left(\frac{1}{q_x} - \frac{1}{\sqrt{\frac{\sigma}{\kappa}+q_x^2}}\right), \quad (1)$$

where k_B is the Boltzmann constant, T is temperature, and L is mean circumference of the erythrocyte contour. This model considers only cell fluctuations at the equatorial plane. From Eq. 1 we extracted bending modulus, tension, and equatorial radius of cells. When fitting the fluctuation data, we considered modes 5-14 in which Eq. 1 was a good representation of the spectrum. Low mode numbers (< 5) were excluded due to significant influence of the cell shape and high mode numbers (>14) had noise in the spectra. In this range, Eq. 1 has limiting behaviours: tension dominates at low mode, $\langle h(q_x, y=0)^2\rangle \sim q^{-1}$ for $(\sigma \gg \kappa q_x^2)$; instead, bending modulus dominates at high q, $\langle h(q_x, y=0)^2\rangle \sim q^{-3}$ for $(\sigma \ll \kappa q_x^2)$. Examples of flickering spectra are reported in Figure S4B.

The dynamics of the fluctuations can also be quantified [38]. We calculated the autocorrelation function of the modes, averaged over 10000 frames. This analysis worked well on modes 7 to 11, higher modes decayed too fast to be fitted. Since we only image the contour of the cell, and therefore probe only modes as a function of their mode component q_x, the timescales of decay of this function are called and can be fitted by:

$$C_{q_x}(t) = \langle h_{q_x}(t') h_{q_x}(t'+t)\rangle_{t'} = \frac{\int dq_y \langle h_{\vec{q}}^2\rangle e^{(-t/\tau_{\vec{q}})}}{\int dq_y \langle h_{\vec{q}}^2\rangle}, \quad (2)$$

where the timescale τ_{q_x} is in general given by

$$\frac{1}{\tau_{q_x}} = \frac{2\gamma + \sigma q^2 + \kappa q^4}{2\left(\frac{\eta_M}{R^2} + q\eta_{int} + q\eta_{ext}\right)}. \quad (3)$$

Eq. 3 gives the relaxation timescale of the modes of a two-dimensional membrane, as a function of the wave vectors; η_M is the two-dimensional membrane viscosity, η_{int} and η_{ext} are the viscosities of the fluid on either side of the membrane, R is the radius of the cell membrane. Two-dimensional phospholipid bilayers have viscosities η_M <10^{-9} N s m^{-1} for temperatures above room T, and $\eta_{ext} \cong 10^{-3}$ Pa s, therefore η_{int} dominates the denominator of Eq.3, i.e. we are able to measure from this procedure the internal viscosity of the RBC. Finally, from τ_{q_x}, using the values of κ and σ obtained from the static spectrum of the same cell in Eq. 1, we then obtained the value of the internal viscosity of the RBC.

Microsphiltration

Parasites were treated with Rapamycin/DMSO at ring stages. At 30-35 hpi in the next cycle when parasitemia was approximately 5%, the two samples were divided into two 1mL samples and diluted to 2% haematocrit, then stained with either Hoechst 33342 (NEB) diluted 1:2000 or SybrGreen diluted 1:10000, for 30 minutes at 37°C. After washing 3x with 1mL PBS, RAP and DMSO-treated lines were mixed 1:1 in duplicate – one Hoechst-RAP:Sybrgreen-DMSO, and one Sybrgreen-RAP:Hoechst-DMSO. The microsphiltration tips were prepared as described previously [40]. 150mg of calibrated metal microspheres (96.50% tin, 3.00% silver, and 0.50% copper; Industrie des Poudres Sphériques) of the 2 different size distributions (5–15 µm or 15–25 µm in diameter) were combined together and resuspended in 1mL RPMI. This was quickly resuspended then pipetted onto the filter of an inverted pipette tip (VWR), which had approximately 1.5cm from the tip cut off. This was connected to a 2-way stopcock by inserting tubing fittings into the tip to create an air-tight seal, and connecting with plastic tubing. The stopcock was connected to a 20mL syringe containing RPMI, which was placed in an electric pump (*kd*Scientific, model Legato 110). To wash the beads, 5mL of RPMI was perfused through the tip at 1mL/min. With a 1mL syringe, 600uL of parasite culture was inserted into the tip using the 2-way stopcock. 6mL of RPMI was then perfused through the tip at a flow rate of 1ml/min. Both the upstream (before microsphiltration) and downstream (flowthrough) were fixed in 4% paraformaldehyde/0.2% glutaraldehyde in PBS for 1h. Samples were immediately analysed by flow cytometry to prevent mixing of the dyes, using a BD LSR Fortessa cell analyser. Hoechst fluorescence was detected using a 355nm (UV) excitation laser with a 450/50nm bandpass filter, while Sybrgreen fluorescence was detected with a 488nm (blue) excitation laser, a 505nm longpass filter and a 530/30nm bandpass filter. The number of infected cells stained by each dye was analysed by FlowJo, and a before/after ratio calculated for both the RAP and DMSO parasites in each of the duplicates. Due to variation between tips, retention by the beads in the RAP/DMSO- treated NF54 and FIKK4.1 lines was compared in paired ANOVA multiple comparison analyses for each tip individually, n=10 including the two technical replicates across five biological replicates.

qRT-PCR

RNA from NF54 parental wild type line and transgenic FIKK4.1 synchronized ring stage parasites was extracted with Trizol following the manufacturer's instructions (RNeasy Minikit, Qiagen). cDNA synthesis

was performed by random primers after DNase I treatment (TURBO DNase, Ambion) using the Super Script III First Stand Synthetis system (from Invitrogen). Primers pairs to analyze *var* gene expression have been described previously [69]. Quantitative real time PCR reactions were performed on a CFX 96 thermocycler (Biorad). Transcriptional level of each *var* gene was normalized using the house keeping control gene *seryl tRNA transferase* (PlasmoDB: PF07_ 0073).

Cytoadhesion assay

Circles large enough to accommodate a sample size of 20µl were drawn at the bottom of a Petri dish using a delimiting Dako pen (Agilent Technologies). 20µl of CSA (Sigma-Aldrich) (1mg/ml in PBS) or 1% BSA control (BSA Fraction V, Sigma-Aldrich) in PBS were added to each spot and left to incubate for at least 3 hours at 4°C. Spots were then washed 3 times with PBS and blocked with 1% BSA in PBS for an hour at room temperature. After 3 additional washes with PBS, 20µl of a suspension of magnet purified trophozoite iRBCs (30-34hpi) at 1.10^6 parasites/ml in PBS was applied to each spot and allowed to settle for one hour at room temperature. Unbound RBCs were washed off the Petri dish by gently adding 25ml of PBS to the centre of the Petri dish followed by 2 minutes rocking on an orbital shaker (50rpm). After 5 washes, bound cells were fixed with 2% glutaraldehyde in PBS for at least 2 hours at 4°C. Glutaraldehyde was removed from the Petri dish with a final wash with PBS. Phase contrast images of spots were collected using an EVOS™ XL inverted microscope. Bound cells were counted using the Analysis Particles tool in Fiji (size = 10 – 200 pixels, circularity = 0.2 – 1.00). The results were statistically tested with a two-way ANOVA test plus a multiple comparison Sidak test comparing all means in GraphPad Prism® 8. The data presented are as mean±SEM.

SEM

Parasites were synchronized to a 1h window then RAP/DMSO-treated at ring stage. 5 days after treatment at ~40hpi, iRBCs were purified by magnetic enrichment. Approximately 10 x 10^6 iRBCs were fixed in 2.5% gluteraldehyde / 4% formaldehyde in PBS for 1h at 37°C, then washed 2x with PBS and resuspended in 200uL PBS. 13mm coverslips were coated with Poly-L lysine for 15 minutes then washed with dH2O and left to dry for 1h. 50uL of the iRBCs suspension was added to the dry coverslips and allowed to settle for 10 minutes. Unattached cells were removed by gentle washing with 2x PBS then 2x dH2O. iRBCs were dehydrated by washing with 70% EtOH, 90% EtOH, then 100% EtOH for 5 minutes each, without allowing

the cells to dry. The coverslips were submerged in Acetone then dried in a Leica EM CPD300 critical point drier. Coverslips were attached to stubs then coated with 4nm of platinum using a Quorum 150R S sputter coater, then imaged using a Phenom ProX scanning tunneling microscope.

Electron micrographs of knobs

3 ul of mature FIKK4.1 KO schizonts (50 % haematocrit) were applied to a glow-discharged (35 mA/30 sec) carbon-coated, copper (200 mesh) finder grid (EMS) and incubated at room temperature for 1 min. Grids were blotted to remove excess cells and washed twice in Tris-buffered saline (TBS) (Sigma), blotting after each wash. Cells were lysed by passing the grid in and out of the meniscus of a drop of 30x diluted TBS for 1 min. After blotting excess buffer, grids were stained with 2 % (w/v) uranyl acetate before blotting dry. Wild-type 3D7 cells were prepared using the same method, but 10 um gold fiducials were also applied to the grids prior to staining. Grids were mounted on a Model 2040 dual-axis tomography holder (Fischione Instruments) and membrane patches were located at low magnification using a Tecnai T12 120 kV electron microscope (FEI) equipped with a 4kx4k Ultrascan 4000 CCD camera (Gatan). Dual-axis tilt series were acquired at a magnification of x42000 (2.56 Å/pixel) from -60° to +60° with an increment of 2° using SerialEM [70]. Processing was carried out using the eTomo workflow from IMOD [71-73]. Images were aligned using either patch tracking or tracking of the gold fiducials for the FIKK4.1 KO or wild-type 3D7 samples, respectively. Tomograms were reconstructed by back-projection with 15 rounds of simultaneous iterative reconstruction technique-like (SIRT-like) filtering. Non-anisotropic diffusion filtering (K=50, iterations=25) was applied to the final trimmed tomograms. Averages of 5 Z slices were produced using Slicer in 3dmod [72].

VAR2CSA surface expression

Cytoadhesion experiments and VAR2CSA surface expression by flow cytometry were performed on RAP/DMSO treated and magnet purified parasites. Cells were diluted to 3x 10.6 cells/ml and 100uL of each sample was distributed into 96-well plates, including one unlabeled and secondary-only control. iRBCs were washed with PBS then resuspended in 1% BSA in PBS for 1h. The plate was centrifuged at 1200rpm for 1 minute, the supernatant was removed and iRBCs were resuspended in 50uL of Rabbit anti-VAR2CSA antibody diluted 1/100 in 1% BSA in PBS, and agitated at 50rpm for 1h. After centrifugation and 2x washes with 1% BSA in PBS, the iRBCs were resuspended in 50uL of anti-rabbit PE diluted 1/100 in 1% BSA in

PBS and kept in the dark for 1h. iRBCs were washed twice with PBS before fixing with 4% paraformaldehyde, 0.2% glutaraldehyde in PBS for 1h. After washing, parasites were stained with Hoechst (1:1000 in PBS) for 30 minutes before flow cytometry using high-throughput acquisition on a BD LSR Fortessa cell analyser. PE fluorescence was detected with a 561nm (yellow) excitation laser and a 586/15 bandpass filter. Using FlowJo software, the population was first gated on Hoechst-positive infected parasites, before the median fluorescent intensity of the PE-fluorescence was calculated for each line. Due to the variation in fluorescence intensity between different experiments, the ratio of RAP/DMSO fluorescence intensity was calculated for each experiment (n=4 for FIKK4.1 and FIKK10.2, n=3 for NF54), and the ratio for NF54, FIKK4.1 and FIKK10.2 compared by multiple comparison ANOVA using Graphpad Prism.

References

1 Baruch, D. I., Gormely, J. A., Ma, C., Howard, R. J. & Pasloske, B. L. Plasmodium falciparum erythrocyte membrane protein 1 is a parasitized erythrocyte receptor for adherence to CD36, thrombospondin, and intercellular adhesion molecule 1. *Proc Natl Acad Sci U S A* **93**, 3497-3502 (1996).

2 Salanti, A. *et al.* Evidence for the involvement of VAR2CSA in pregnancy-associated malaria. *J Exp Med* **200**, 1197-1203, doi:10.1084/jem.20041579 (2004).

3 Marti, M., Good, R. T., Rug, M., Knuepfer, E. & Cowman, A. F. Targeting malaria virulence and remodeling proteins to the host erythrocyte. *Science* **306**, 1930-1933, doi:10.1126/science.1102452 (2004).

4 Hiller, N. L. *et al.* A host-targeting signal in virulence proteins reveals a secretome in malarial infection. *Science* **306**, 1934-1937, doi:10.1126/science.1102737 (2004).

5 Spielmann, T. & Gilberger, T. W. Protein export in malaria parasites: do multiple export motifs add up to multiple export pathways? *Trends Parasitol* **26**, 6-10, doi:10.1016/j.pt.2009.10.001 (2010).

6 Kriek, N. *et al.* Characterization of the pathway for transport of the cytoadherence-mediating protein, PfEMP1, to the host cell surface in malaria parasite-infected erythrocytes. *Mol Microbiol* **50**, 1215-1227 (2003).

7 Maier, A. G. *et al.* Exported proteins required for virulence and rigidity of Plasmodium falciparum-infected human erythrocytes. *Cell* **134**, 48-61, doi:10.1016/j.cell.2008.04.051 (2008).

8 Oberli, A. *et al.* Plasmodium falciparum Plasmodium helical interspersed subtelomeric proteins contribute to cytoadherence and anchor P. falciparum erythrocyte membrane protein 1 to the host cell cytoskeleton. *Cellular Microbiology* **18**, 1415-1428, doi:10.1111/cmi.12583 (2016).

9 Proellocks, N. I. *et al.* A lysine-rich membrane-associated PHISTb protein involved in alteration of the cytoadhesive properties of Plasmodium falciparum-infected red blood cells. *FASEB J* **28**, 3103-3113, doi:10.1096/fj.14-250399 (2014).

10 Salomao, M. *et al.* Protein 4.1R-dependent multiprotein complex: new insights into the structural organization of the red blood cell membrane. *Proc Natl Acad Sci U S A* **105**, 8026-8031, doi:10.1073/pnas.0803225105 (2008).

11 Lux, S. E. Anatomy of the red cell membrane skeleton: unanswered questions. *Blood* **127**, 187-199, doi:10.1182/blood-2014-12-512772 (2016).

12 Glenister, F. K., Coppel, R. L., Cowman, A. F., Mohandas, N. & Cooke, B. M. Contribution of parasite proteins to altered mechanical properties of malaria-infected red blood cells. *Blood* **99**, 1060-1063, doi:10.1182/blood.V99.3.1060 (2002).

13 Crabb, B. S. *et al.* Targeted gene disruption shows that knobs enable malaria-infected red cells to cytoadhere under physiological shear stress. *Cell* **89**, 287-296, doi:10.1016/s0092-8674(00)80207-x (1997).

14 Otto, T. D. *et al.* Genome sequencing of chimpanzee malaria parasites reveals possible pathways of adaptation to human hosts. *Nature communications* **5**, 4754, doi:10.1038/ncomms5754 (2014).

15 Ward, P., Equinet, L., Packer, J. & Doerig, C. Protein kinases of the human malaria parasite Plasmodium falciparum: the kinome of a divergent eukaryote. *BMC Genomics* **5**, 79, doi:10.1186/1471-2164-5-79 (2004).

937 16 Schneider, A. G. & Mercereau-Puijalon, O. A new Apicomplexa-specific protein kinase
938 family: multiple members in Plasmodium falciparum, all with an export signature. *BMC*
939 *Genomics* **6**, 30, doi:10.1186/1471-2164-6-30 (2005).
940 17 Lin, B. C. *et al.* The anthraquinone emodin inhibits the non-exported FIKK kinase from
941 Plasmodium falciparum. *Bioorg Chem* **75**, 217-223, doi:10.1016/j.bioorg.2017.09.011
942 (2017).
943 18 Nunes, M. C., Goldring, J. P., Doerig, C. & Scherf, A. A novel protein kinase family in
944 Plasmodium falciparum is differentially transcribed and secreted to various cellular
945 compartments of the host cell. *Mol Microbiol* **63**, 391-403, doi:10.1111/j.1365-
946 2958.2006.05521.x (2007).
947 19 Brandt, G. S. & Bailey, S. Dematin, a human erythrocyte cytoskeletal protein, is a substrate
948 for a recombinant FIKK kinase from Plasmodium falciparum. *Mol Biochem Parasitol* **191**,
949 20-23, doi:10.1016/j.molbiopara.2013.08.003 (2013).
950 20 Osman, K. T. *et al.* Biochemical characterization of FIKK8--A unique protein kinase from
951 the malaria parasite Plasmodium falciparum and other apicomplexans. *Mol Biochem*
952 *Parasitol* **201**, 85-89, doi:10.1016/j.molbiopara.2015.06.002 (2015).
953 21 Kats, L. M. *et al.* An exported kinase (FIKK4.2) that mediates virulence-associated changes
954 in Plasmodium falciparum-infected red blood cells. *Int J Parasitol* **44**, 319-328,
955 doi:10.1016/j.ijpara.2014.01.003 (2014).
956 22 Nunes, M. C., Okada, M., Scheidig-Benatar, C., Cooke, B. M. & Scherf, A. Plasmodium
957 falciparum FIKK kinase members target distinct components of the erythrocyte
958 membrane. *PLoS One* **5**, e11747, doi:10.1371/journal.pone.0011747 (2010).
959 23 Sundararaman, S. A. *et al.* Genomes of cryptic chimpanzee Plasmodium species reveal
960 key evolutionary events leading to human malaria. *Nature communications* **7**, 11078,
961 doi:10.1038/ncomms11078
962 10.1038/ncomms11078.</p> (2016).
963 24 Moon, R. W. *et al.* Adaptation of the genetically tractable malaria pathogen Plasmodium
964 knowlesi to continuous culture in human erythrocytes. *Proc Natl Acad Sci U S A* **110**, 531-
965 536, doi:10.1073/pnas.1216457110 (2013).
966 25 Thompson, A. *et al.* Tandem mass tags: a novel quantification strategy for comparative
967 analysis of complex protein mixtures by MS/MS. *Anal Chem* **75**, 1895-1904 (2003).
968 26 Kim, C. C., Wilson, E. B. & DeRisi, J. L. Improved methods for magnetic purification of
969 malaria parasites and haemozoin. *Malaria journal* **9**, 17-17, doi:10.1186/1475-2875-9-17
970 (2010).
971 27 Jones, M. L. *et al.* A versatile strategy for rapid conditional genome engineering using loxP
972 sites in a small synthetic intron in Plasmodium falciparum. *Sci Rep* **6**, 21800,
973 doi:10.1038/srep21800 (2016).
974 28 Birnbaum, J. *et al.* A genetic system to study Plasmodium falciparum protein function.
975 *Nat Methods* **14**, 450-456, doi:10.1038/nmeth.4223 (2017).
976 29 Collins, C. R. *et al.* Robust inducible Cre recombinase activity in the human malaria
977 parasite Plasmodium falciparum enables efficient gene deletion within a single asexual
978 erythrocytic growth cycle. *Mol Microbiol* **88**, 687-701, doi:10.1111/mmi.12206 (2013).
979 30 Thomas, J. A. *et al.* Development and Application of a Simple Plaque Assay for the Human
980 Malaria Parasite Plasmodium falciparum. *PLoS One* **11**, e0157873,
981 doi:10.1371/journal.pone.0157873 (2016).

982 31 Bouyer, G. *et al.* Plasmodiumfalciparum infection induces dynamic changes in the
983 erythrocyte phospho-proteome. *Blood Cells Mol Dis* **58**, 35-44,
984 doi:10.1016/j.bcmd.2016.02.001 (2016).
985 32 da Silva, F. L. *et al.* A Plasmodium falciparum S33 proline aminopeptidase is associated
986 with changes in erythrocyte deformability. *Exp Parasitol* **169**, 13-21,
987 doi:10.1016/j.exppara.2016.06.013 (2016).
988 33 Charnaud, S. C. *et al.* The exported chaperone Hsp70-x supports virulence functions for
989 Plasmodium falciparum blood stage parasites. *PLoS One* **12**, e0181656,
990 doi:10.1371/journal.pone.0181656 (2017).
991 34 Horrocks, P. *et al.* PfEMP1 expression is reduced on the surface of knobless Plasmodium
992 falciparum infected erythrocytes. *J Cell Sci* **118**, 2507-2518, doi:10.1242/jcs.02381 (2005).
993 35 Waterkeyn, J. G. *et al.* Targeted mutagenesis of Plasmodium falciparum erythrocyte
994 membrane protein 3 (PfEMP3) disrupts cytoadherence of malaria-infected red blood
995 cells. *EMBO J* **19**, 2813-2823, doi:10.1093/emboj/19.12.2813 (2000).
996 36 Goel, S. *et al.* RIFINs are adhesins implicated in severe Plasmodium falciparum malaria.
997 *Nat Med* **21**, 314-317, doi:10.1038/nm.3812 (2015).
998 37 Regev-Rudzki, N. *et al.* Cell-cell communication between malaria-infected red blood cells
999 via exosome-like vesicles. *Cell* **153**, 1120-1133, doi:10.1016/j.cell.2013.04.029 (2013).
1000 38 Yoon, Y. Z. *et al.* Flickering analysis of erythrocyte mechanical properties: dependence on
1001 oxygenation level, cell shape, and hydration level. *Biophys J* **97**, 1606-1615,
1002 doi:10.1016/j.bpj.2009.06.028 (2009).
1003 39 Koch, M. *et al.* Plasmodium falciparum erythrocyte-binding antigen 175 triggers a
1004 biophysical change in the red blood cell that facilitates invasion. *Proc Natl Acad Sci U S A*
1005 **114**, 4225-4230, doi:10.1073/pnas.1620843114 (2017).
1006 40 Lavazec, C. *et al.* Microsphiltration: a microsphere matrix to explore erythrocyte
1007 deformability. *Methods Mol Biol* **923**, 291-297, doi:10.1007/978-1-62703-026-7_20
1008 (2013).
1009 41 Watermeyer, J. M. *et al.* A spiral scaffold underlies cytoadherent knobs in Plasmodium
1010 falciparum-infected erythrocytes. *Blood* **127**, 343-351, doi:10.1182/blood-2015-10-
1011 674002 (2016).
1012 42 Wu, Y. *et al.* Identification of phosphorylated proteins in erythrocytes infected by the
1013 human malaria parasite Plasmodium falciparum. *Malaria Journal* **8**, 105,
1014 doi:10.1186/1475-2875-8-105 (2009).
1015 43 Shi, H. *et al.* Life cycle-dependent cytoskeletal modifications in Plasmodium falciparum
1016 infected erythrocytes. *PloS One* **8**, e61170, doi:10.1371/journal.pone.0061170 (2013).
1017 44 Nash, G. B., O'Brien, E., Gordon-Smith, E. C. & Dormandy, J. A. Abnormalities in the
1018 mechanical properties of red blood cells caused by Plasmodium falciparum. *Blood* **74**,
1019 855-861 (1989).
1020 45 Staines, H. M. *et al.* Electrophysiological studies of malaria parasite-infected erythrocytes:
1021 Current status. *International Journal for Parasitology* **37**, 475-482,
1022 doi:10.1016/j.ijpara.2006.12.013 (2007).
1023 46 Mata-Cantero, L. *et al.* New insights into host-parasite ubiquitin proteome dynamics in P.
1024 falciparum infected red blood cells using a TUBEs-MS approach. *Journal of Proteomics*
1025 **139**, 45-59, doi:10.1016/j.jprot.2016.03.004 (2016).
1026 47 Millholland, M. G. *et al.* A host GPCR signaling network required for the cytolysis of
1027 infected cells facilitates release of apicomplexan parasites. *Cell Host Microbe* **13**, 15-28,
1028 doi:10.1016/j.chom.2012.12.001 (2013).

1029 48 Zuccala, E. S. *et al.* Quantitative phospho-proteomics reveals the Plasmodium merozoite
1030 triggers pre-invasion host kinase modification of the red cell cytoskeleton. *Sci Rep* **6**,
1031 19766, doi:10.1038/srep19766 (2016).
1032 49 Sisquella, X. *et al.* Plasmodium falciparum ligand binding to erythrocytes induce
1033 alterations in deformability essential for invasion. *Elife* **6**, doi:10.7554/eLife.21083 (2017).
1034 50 Davies, H. M., Thalassinos, K. & Osborne, A. R. Expansion of Lysine-rich Repeats in
1035 Plasmodium Proteins Generates Novel Localization Sequences That Target the Periphery
1036 of the Host Erythrocyte. *J. Biol. Chem.* **291**, 26188-26207, doi:10.1074/jbc.M116.761213
1037 (2016).
1038 51 Zhang, M. *et al.* Uncovering the essential genes of the human malaria parasite
1039 Plasmodium falciparum by saturation mutagenesis. *Science* **360**,
1040 doi:10.1126/science.aap7847 (2018).
1041 52 Tiburcio, M. *et al.* A switch in infected erythrocyte deformability at the maturation and
1042 blood circulation of Plasmodium falciparum transmission stages. *Blood* **119**, e172-180,
1043 doi:10.1182/blood-2012-03-414557 (2012).
1044 53 Naissant, B. *et al.* Plasmodium falciparum STEVOR phosphorylation regulates host
1045 erythrocyte deformability enabling malaria parasite transmission. *Blood* **127**, e42-53,
1046 doi:10.1182/blood-2016-01-690776 (2016).
1047 54 Aingaran, M. *et al.* Host cell deformability is linked to transmission in the human malaria
1048 parasite Plasmodium falciparum. *Cell Microbiol* **14**, 983-993, doi:10.1111/j.1462-
1049 5822.2012.01786.x (2012).
1050 55 Madeira, F. *et al.* The EMBL-EBI search and sequence analysis tools APIs in 2019. *Nucleic*
1051 *acids research*, doi:10.1093/nar/gkz268 (2019).
1052 56 Guindon, S. *et al.* New algorithms and methods to estimate maximum-likelihood
1053 phylogenies: assessing the performance of PhyML 3.0. *Syst. Biol.* **59**, 307-321,
1054 doi:10.1093/sysbio/syq010 (2010).
1055 57 Rambaut, A. FigTree v1.4.2. (2014).
1056 58 Trager, W. & Jensen, J. B. Human malaria parasites in continuous culture. *Science* **193**,
1057 673-675 (1976).
1058 59 Cox, J. & Mann, M. MaxQuant enables high peptide identification rates, individualized
1059 p.p.b.-range mass accuracies and proteome-wide protein quantification. *Nat Biotechnol*
1060 **26**, 1367-1372, doi:10.1038/nbt.1511 (2008).
1061 60 Cox, J. *et al.* Andromeda: a peptide search engine integrated into the MaxQuant
1062 environment. *J Proteome Res* **10**, 1794-1805, doi:10.1021/pr101065j (2011).
1063 61 Tyanova, S. *et al.* The Perseus computational platform for comprehensive analysis of
1064 (prote)omics data. *Nature Methods* **13**, 731-740, doi:10.1038/nmeth.3901 (2016).
1065 62 Love, M. I., Huber, W. & Anders, S. Moderated estimation of fold change and dispersion
1066 for RNA-seq data with DESeq2. *Genome Biol* **15**, 550, doi:10.1186/s13059-014-0550-8
1067 (2014).
1068 63 Domaszewska, T. *et al.* Concordant and discordant gene expression patterns in mouse
1069 strains identify best-fit animal model for human tuberculosis. *Sci Rep* **7**, 12094,
1070 doi:10.1038/s41598-017-11812-x (2017).
1071 64 Kulzer, S. *et al.* Plasmodium falciparum-encoded exported hsp70/hsp40 chaperone/co-
1072 chaperone complexes within the host erythrocyte. *Cell Microbiol* **14**, 1784-1795,
1073 doi:10.1111/j.1462-5822.2012.01840.x (2012).

65 Shannon, P. *et al.* Cytoscape: a software environment for integrated models of biomolecular interaction networks. *Genome Research* **13**, 2498-2504, doi:10.1101/gr.1239303 (2003).
66 Wagih, O., Sugiyama, N., Ishihama, Y. & Beltrao, P. Uncovering Phosphorylation-Based Specificities through Functional Interaction Networks. *Mol Cell Proteomics* **15**, 236-245, doi:10.1074/mcp.M115.052357 (2016).
67 Pecreaux, J., Dobereiner, H. G., Prost, J., Joanny, J. F. & Bassereau, P. Refined contour analysis of giant unilamellar vesicles. *Eur Phys J E Soft Matter* **13**, 277-290, doi:10.1140/epje/i2004-10001-9 (2004).
68 Shimobayashi, S. F. *et al.* Direct measurement of DNA-mediated adhesion between lipid bilayers. *Phys Chem Chem Phys* **17**, 15615-15628, doi:10.1039/c5cp01340b (2015).
69 Rask, T. S., Hansen, D. A., Theander, T. G., Gorm Pedersen, A. & Lavstsen, T. Plasmodium falciparum erythrocyte membrane protein 1 diversity in seven genomes--divide and conquer. *PLoS Comput Biol* **6**, doi:10.1371/journal.pcbi.1000933 (2010).
70 Mastronarde, D. N. SerialEM: A Program for Automated Tilt Series Acquisition on Tecnai Microscopes Using Prediction of Specimen Position. *Microscopy and Microanalysis* **9**, 1182-1183, doi:10.1017/S1431927603445911 (2003).
71 Kremer, J. R., Mastronarde, D. N. & McIntosh, J. R. Computer visualization of three-dimensional image data using IMOD. *J Struct Biol* **116**, 71-76, doi:10.1006/jsbi.1996.0013 (1996).
72 Mastronarde, D. N. Dual-axis tomography: an approach with alignment methods that preserve resolution. *J Struct Biol* **120**, 343-352, doi:10.1006/jsbi.1997.3919 (1997).
73 Mastronarde, D. N. & Held, S. R. Automated tilt series alignment and tomographic reconstruction in IMOD. *J Struct Biol* **197**, 102-113, doi:10.1016/j.jsb.2016.07.011 (2017).

Acknowledgements:

We would like to thank Helen R. Saibil, Pietro Cicuta, Mike J. Blackman and Anthony A. Holder for critical feedback on the manuscript, and members of the Treeck, Blackman and Holder labs for discussions throughout. We also thank Bram Snijders and Helen Flynn from the Mass-spectrometry Science Technology platform (MS-STP), Anne Weston, Matt Russell and Lucy Collinson from the Electron Microscopy STP, and everyone from the Flow Cytometry STP at the Francis Crick Institute for outstanding technical support and training. Thanks to Alan Cowman for the PTP2 antibody, Jude Przyborski for the Hsp-70x antibody, and Julian Rayner and Lyndsay Parish for the MAHRP1 antibody. We are grateful to Matthew Jones for initial experiments, and Marion Koch and Jake Baum from Imperial College London for performing initial flickering analysis experiments.

This work was supported by funding from The Francis Crick Institute, which receives its core funding from Cancer Research UK (FC001189; FC001999), the UK Medical Research Council (FC001189; FC001999) and the Wellcome Trust (FC001189; FC001999) and an Idea to Innovation Award (FC10550). V.I. is supported by the Engineering and Physical Sciences Research Council (EPSRC) (EP/R011443/1) and the Sackler fellowship. MK receives support from the NIHR Imperial College BRC and the Wellcome Trust (Sir Henry Wellcome Fellowship grant 206508/Z/17/Z). C.B. was supported by an MRC Project Grant (MR/P010288/1). B.G., D.D.S., J.P.S. are supported by the French National Research Agency (ANR-16-CE11-0014-01).

Author Contributions

Conceptualization, H.D., H.B, M.T; Methodology, H.D., H.B, M.T. Software, H.D., X.Y., M.K.; Validation, H.D., H.B; Formal analysis, H.D., H.B., M.B., C.B., X.Y., M.K., M.T.; Investigation, H.D., H.B., M.B., M. Ti., V.I., D.D.S., J.P.S, and C.B.; Resources, M. Ti., B.G., Data curation, X.Y; Writing – original draft, H.D., H.B., M.T., M.B., V.I., C.B., D.D.S. and J.P.S.; Writing – Review and Editing, H.D., H.B., M.B., V.I., C.B., D.D.S., J.P.S., B.G., M.K. and M.T.; Visualization, H.D., H.B., X.Y. and M.T.; Supervision, B.G., M.K. and M.T.; Funding acquisition, M.T.

Declaration of Interests

The authors declare no competing interests

Materials & Correspondence

Correspondence and material requests should be addressed to Moritz Treeck

Tables

Table 1: Proteins identified as FIKK4.1 substrates previously shown to play a role in malaria pathogenesis.

Supplementary Table Titles and Legends

Table S1. TMT quantification of phosphosites - raw data for all experiments

(T1A) Experimental layout of all samples included in the 6 experiments. (T1B-G) Raw data from all TMT mass spectrometry experiments. The data were filtered to remove common contaminants and IDs originating from reverse decoy sequences. To generate a list of all quantified phosphosites reporter intensities were filtered for 1 valid value. The individual reporter intensities, total TMT reporter intensity, mass error, site localization probability, score for identification and posterior error probability (PEP) are shown for each phosphosite.

Table S2. Phosphoproteome of RBC infected with *P. falciparum* and *P. knowlesi*, and comparison of blood types (related to Figure 1)

Analysed data from experiments 1 and 2 (Figure 1). Data are divided by species of origin for each experiment, (T2A and T2C) For phosphosites on human proteins, the log2 fold change between samples, *P*-value, and significance is shown. For experiment 2 (T2C), log2 fold change values above or below ± 2 are also indicated, as it was not possible to calculate *P*-values where some intensities were not observed. The log2-transformed, normalised, and averaged intensity values across replicates is shown. (T2B and T2C) For phosphosites on *P. falciparum* and *P. knowlesi* proteins, only the log2-transformed, normalised, and averaged intensity values across replicates is shown.

Table S3. Phosphoproteome of FIKK knockout parasites (related to Figure 3)

Analysed data from experiments 3, 4, 5, and 6 (Figure 2). (T3A) For phosphosites on both human and *P. falciparum* proteins, the log2 fold change between DMSO and RAP-treated FIKK cKO lines is shown. The Log2 fold change between *P. falciparum* NF54 and *P. knowlesi*-infected RBC is included only for phosphosites on human proteins. The column to the right of the Log2 fold change values for each line indicates whether the change is considered significant (i.e. values above or below ± 4 x standard deviation, which is indicated in the column title for each line). The average Log2 fold change between replicated experiments is included for all replicated lines. (T3B) All phosphosites which were significantly changing upon deletion of any FIKK kinases. (T3C) All phosphosites from human proteins which were observed across all experiments. The Log2 fold change between *P. falciparum* and *P. knowlesi*-infected RBCs from experiment 1 was also included, and the average calculated between all experiments. (T3D-O) All phosphosites which were significantly changing upon deletion of specific FIKK kinases. Phosphosites are sorted on the log2 fold changes occurring upon deletion of the FIKK kinase of interest.

Table S4. Phosphorylation motif for potential FIKK4.1 substrates (related to Figure 4)

A phosphorylation motif was calculated on the most likely candidates for FIKK4.1 substrates. Stringent criteria were applied to exclude false positives. All phosphosites which were significantly less phosphorylated upon deletion of FIKK4.1 in both biological replicates, and which are on either RBC proteins or *P. falciparum* exported proteins are shown. The amino acid at the -3 position to the phosphorylated residue in indicated, and coloured in red if it is either lysine or arginine. The total number, and percentage of phosphosites with either K or R at the -3 position is indicated at the bottom of the table.

Table S5. Primers and synthesised genes used for the generation of FIKK cKO lines, and primers used to confirm correct integration and excision upon RAP-treatment.

(T5A) Synthesised genes containing the recodonised FIKK kinase domain sequences used for the generation of the conditional KO lines. Sequences were either purchased as synthetic genes (from either IDT or Geneart, as indicated), or as Gblocks (IDT). (T5B) Primers used to PCR-amplify the components for each cKO plasmid. Fragments were assembled by Gibson assembly. A different strategy was used for different FIKKs, depending on whether the plasmid would be integrated by selection-linked integration or through CRISPR/Cas9, and on the components included in the synthesised gene. (T5C) Primers used to

confirm correct integration of the plasmid into the FIKK locus, and correct excision of the kinase domain upon RAP-treatment. Primers correspond to those indicated by arrows in Figure S5.

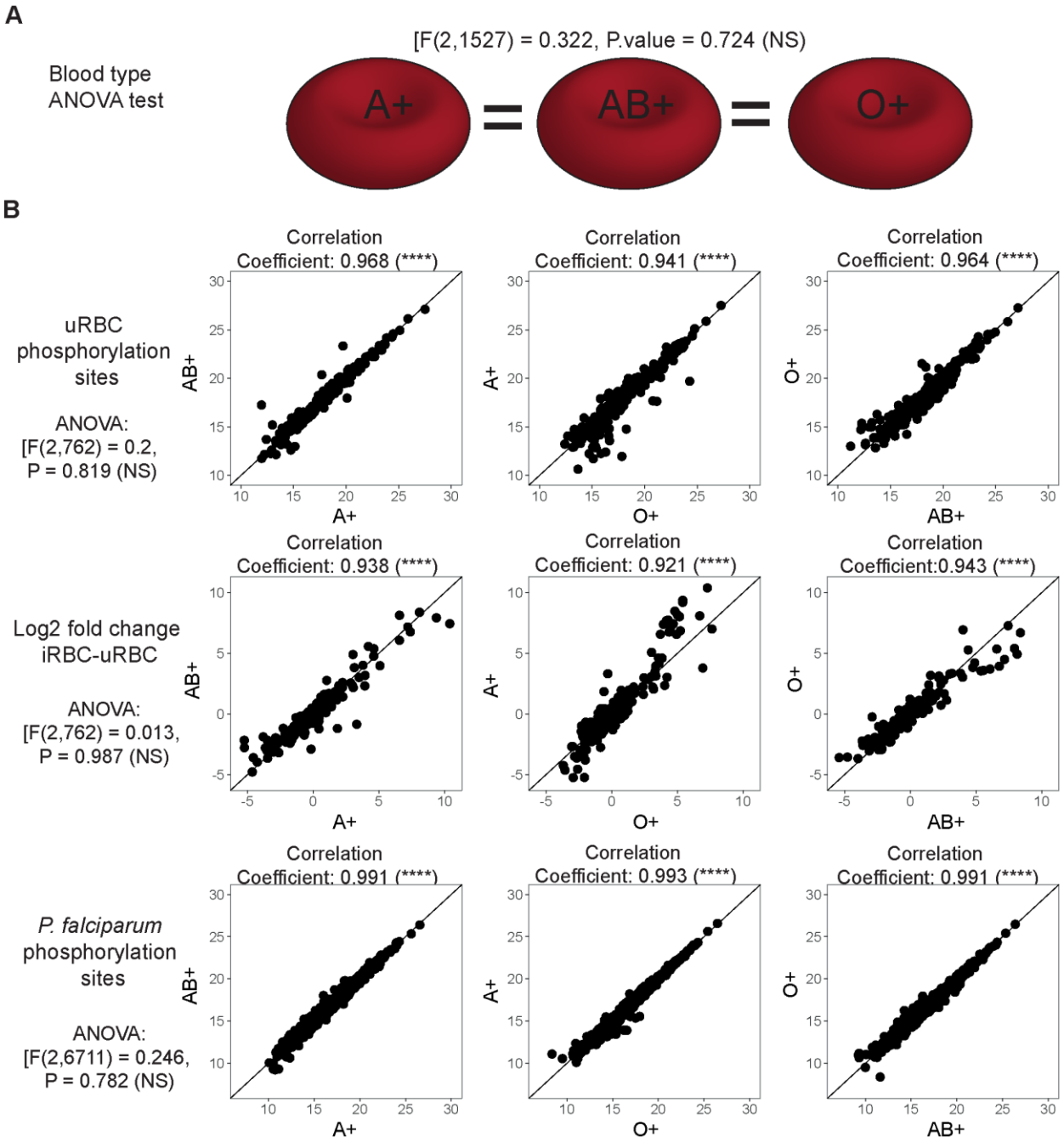

Figure S1: Statistical analysis of phosphorylation on RBC and *P. falciparum* proteins in different blood types. Related to figure 1.
(A) One way ANOVA test. (blood type) Testing the hypothesis that blood type does not affect log2 fold change in RBC phosphorylation upon infection (A+=AB+=O+). F-value: 0.322 >> 0.05, therefore blood type does not affect RBC phosphorylation. (B) Within-sample and species-specific testing of differences between blood types using one way ANOVA tests. Plots show phosphorylation intensity on uRBC proteins, log2 fold change on RBC proteins in iRBC-uRBC, and phosphorylation intensity on *P. falciparum* proteins,

in two different blood types. Therefore there is no significant difference between blood types. Above each plot is the correlation coefficient (R) between the two blood types in the condition tested. There was no significant difference observed in any condition and there was a strong correlation between the phosphosite intensities in all blood types.

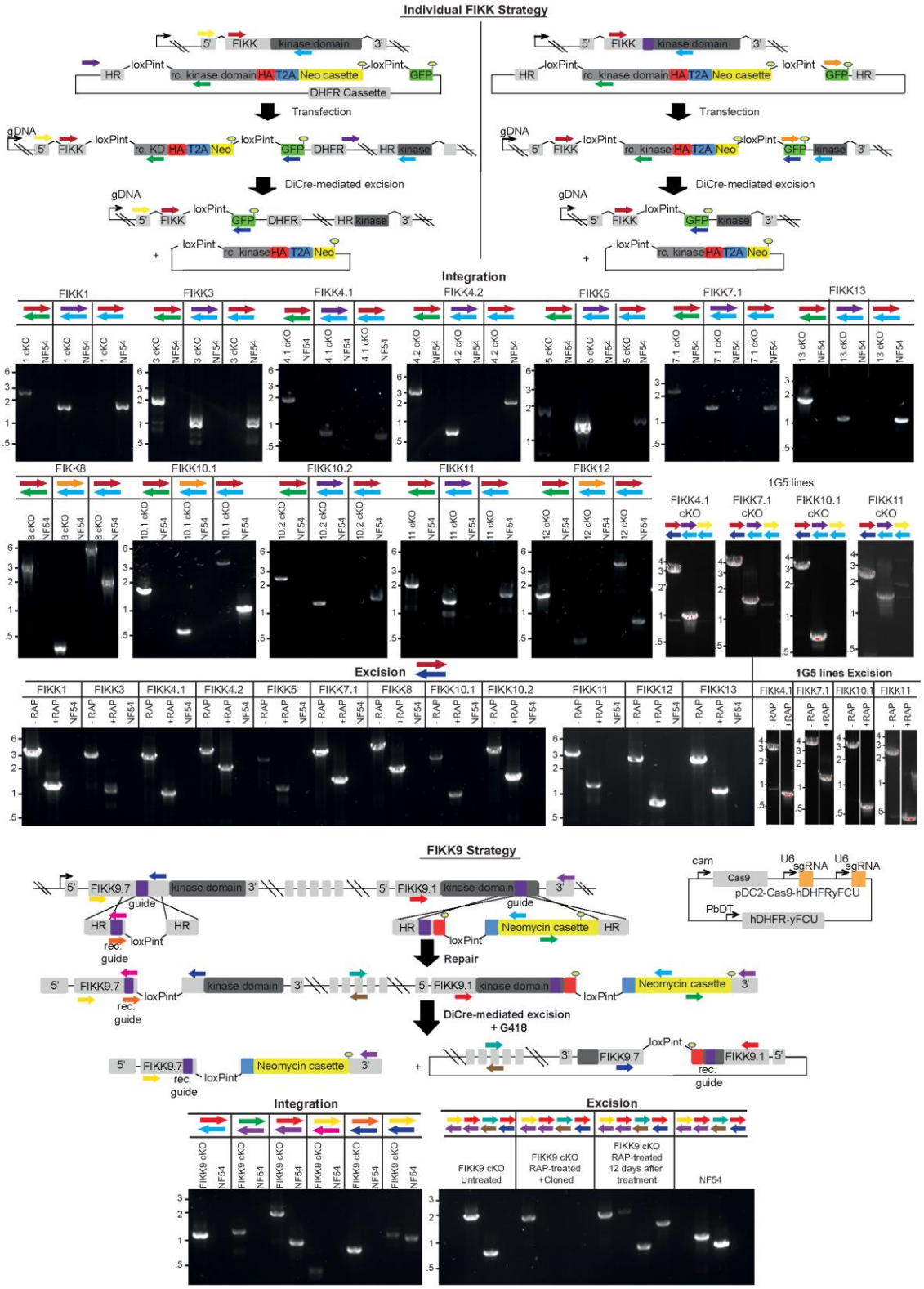

Figure S2: Correct integration of the different FIKK cKO plasmids into the respective endogenous loci and correct excision of their kinase domains upon RAP treatment related to Figure 2.
Schematics describing the different strategies used for generating the conditional FIKK knockout lines by introducing 2 LoxP introns on each side of the recodonised FIKK kinase domain fused to a triple HA tag (red), a T2A skip peptide (blue) and a neomycin-resistance gene. Black arrows represent promoters and lollipops depict STOP codons. The relative positions of primers used to confirm correct integration of the plasmids into the respective loci and correct excision of the FIKK kinase domains upon RAP treatment are shown as coloured arrows. cKO, conditional knockout; DiCre, dimerisable Cre recombinase; GFP, green fluorescent protein; HA, haemagglutinin; HR, homology region; Neo, neomycin-resistance cassette; RAP, rapamycin; rc. KD, recodonised kinase domain; T2A, T2A skip peptide. Alongside the schematics are shown the PCR gels confirming correct integration and correct excision. DNA size markers in kbp are indicated on the left.

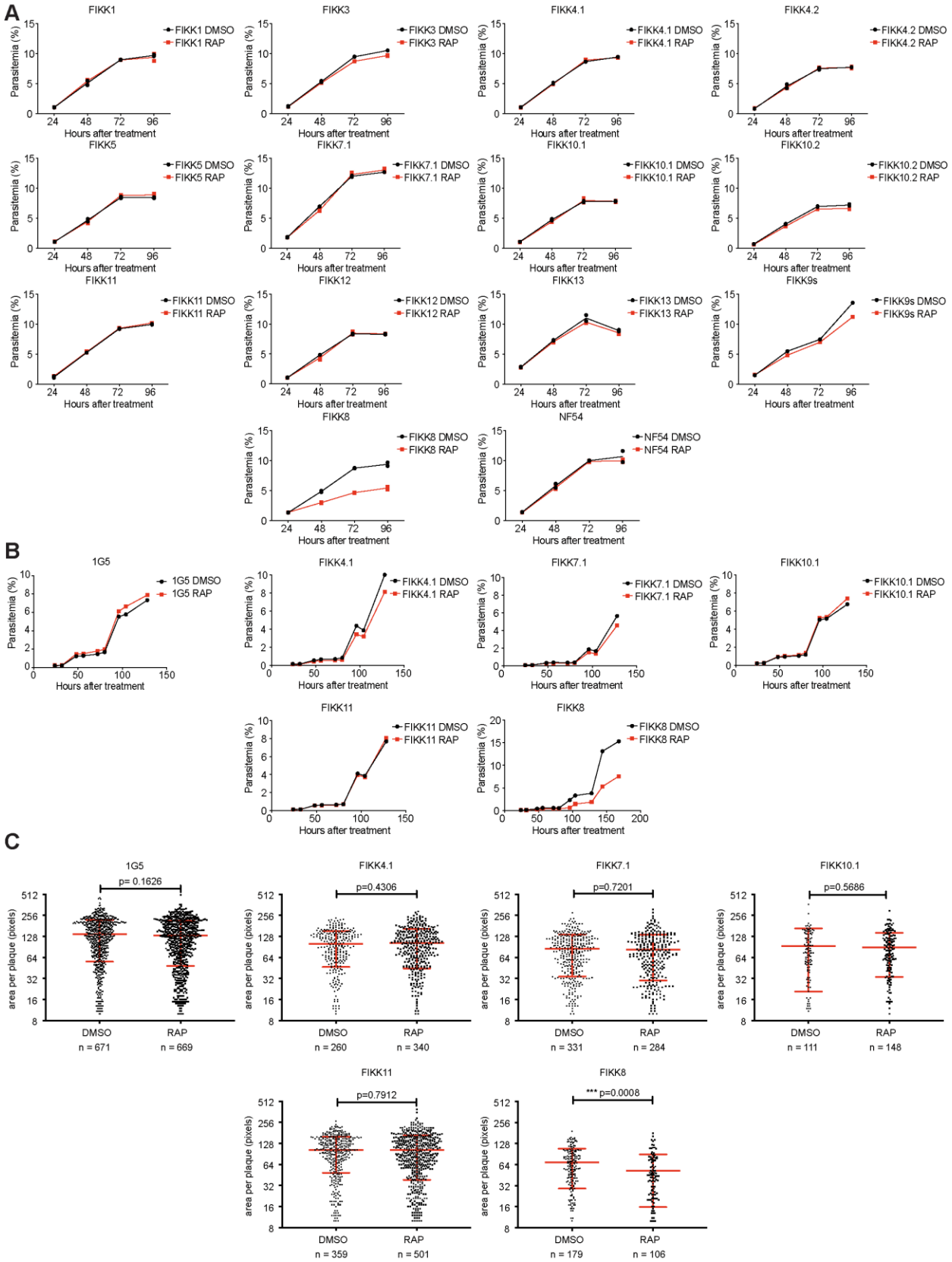

1231

1232

1233

Figure S3: Exported FIKK kinases are not playing a role in parasite growth under standard culture conditions related to Figure 2.

(A) Parasite growth curves for *Plasmodium falciparum* NF54 FIKK conditional knockout lines. Starting parasitemia was adjusted to 1% and samples were fixed every 24 hours for 96 hours. Parasitemia was measured by flow cytometry on 2 biological replicates for all FIKKs, except FIKK13, DMSO- or RAP-treated. Only 1 replicate was measured for FIKK13. Dots represent parasitemia for each replicate for each condition. Lines connect mean of time points for each condition. **(B)** Parasite growth curves for *Plasmodium falciparum* 1G5 FIKK conditional knockout lines. Starting parasitemia was adjusted to 0.1% and samples were fixed every 12 hours for 128 hours. Only 1 replicate was measured by flow cytometry for each time points and for each condition. **(C)** Scatter plots showing the area of plaques obtained by plaque assay for 1G5 FIKK conditional knockout lines, DMSO- (left) or RAP-treated (right). Horizontal bars indicate mean plaque area ± 1SD. n = number of plaque (*** $p<0.001$).

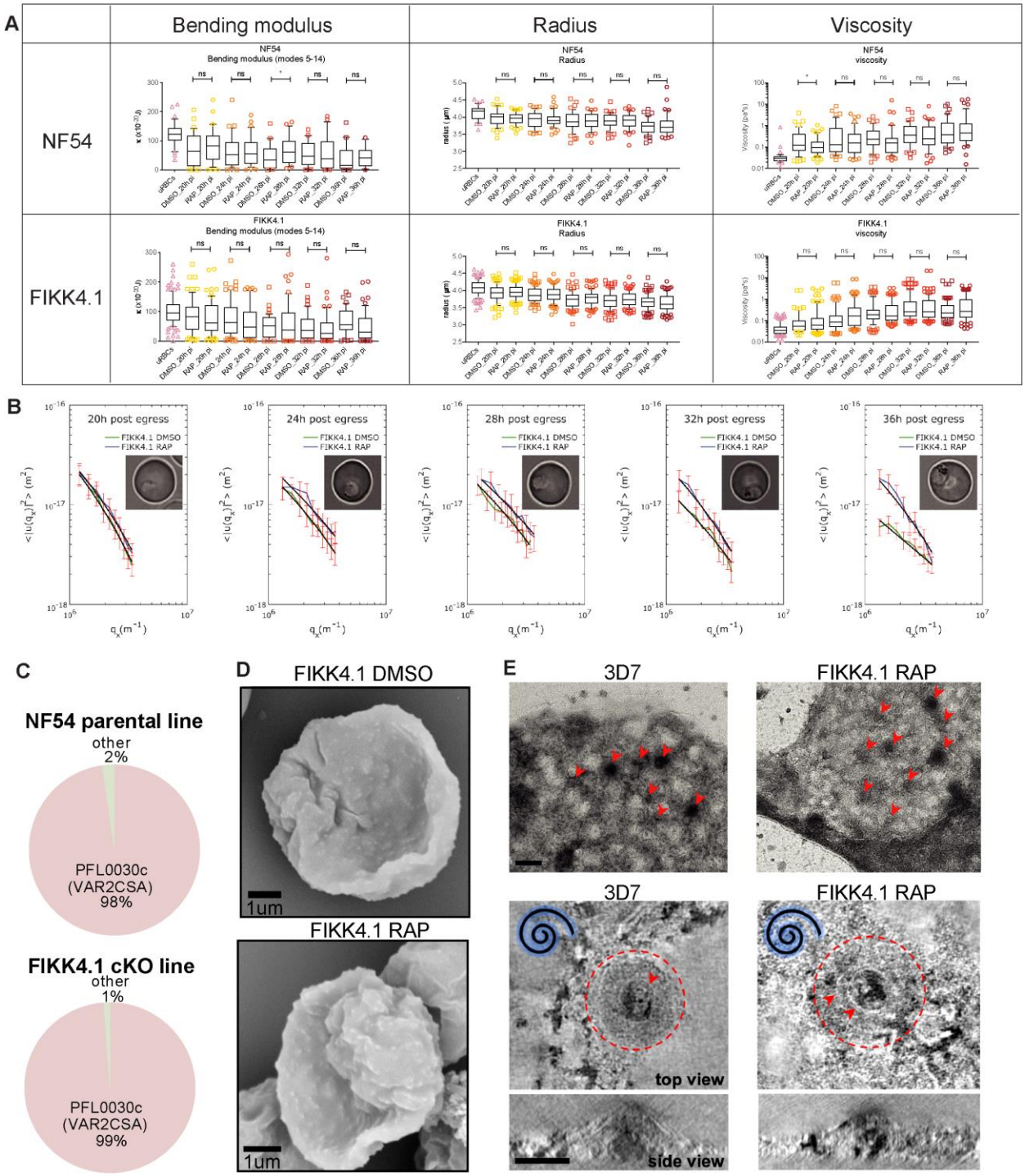

Figure S4: Characterization of FIKK4.1 knockout, related to Figure 5

(A) Time-course flicker spectroscopy comparing the membrane bending modulus, the radius and the viscosity of uRBCs and RBCs infected with NF54::DiCre and FIKK4.1::DiCre DMSO- or RAP- treated parasites. Horizontal line within the box represents the median and whiskers boundaries represent the 10th and 90th percentile (* $p<0.05$) **(B)** Representative flickering spectra of DMSO- (in green) or RAP-treated (in blue) FIKK4.1::DiCre parasites at increasing time post-invasion. Mean square amplitude of fluctuations remains similar for DMSO-treated FIKK4.1::DiCre parasites throughout parasite development, while fluctuations in knockout parasites, i.e. RAP-treated FIKK4.1::DiCre, decrease significantly at 32 and 36 hours post-invasion. Fitted modes 5-14. The error bars are calculated as $SD/\sqrt{(n \times dt)/\tau_{q_x}}$, where *SD* is the standard deviation, *n* total number of frames, *dt* time gap between each frame, and τ_{q_x} the relaxation

time for each mode. **(C)** *Var* gene transcription profile of NF54::DiCre and FIKK4.1::DiCre parasites determined by real-time qPCR. Transcriptional level of each *var* genes were normalized with the housekeeping gene, seryl-tRNAtransferase. **D)** SEM images of the surface of erythrocytes infected with DMSO or RAP-treated FIKK4.1::DiCre parasites (scale bar = 1µm). **(E)**Top panels: Electron micrographs of knobs on detergent treated, negatively-stained RBC ghosts from wild-type 3D7 and FIKK4.1KO schizonts imaged at low-magnification. Red arrows indicate position of knobs, which show up as circular dark patches on the membrane fragment (scale bar = 200 nm). Bottom panels: Negative-stain electron tomography reveals typical structural features of the knob complex. In top views of knobs (XY), the knob-coat is outlined with a red dashed line and the underlying knob spiral is indicated by red arrow heads. In these examples of knobs, the underlying spiral is left-handed (indicated by the blue spiral symbol) showing that the knob is pointing upwards from the plane of the grid. A side view (XZ) of the same knob shows that the height and diameter of the knobs in wild-type 3D7 schizonts FIKK 4.1KO schizonts is similar. Knobs with a right-handed spiral are show in Figure 5F. These knobs are pointing downwards and are compressed against the surface of the grid, hence more rings of the spiral structure are visible in the plane of the tomogram. Images are an average of 5 central slices of the tomogram (scale bar =50 nm).